

# Vertically propagating seiches and standing modes preclusion in a steep-bottom tropical reservoir

Andres Posada-Bedoya<sup>1</sup>, Andrés Gómez Giraldo<sup>2</sup>, and Ricardo Roman-Botero<sup>2</sup>

<sup>1</sup>Queen's University

<sup>2</sup>Universidad Nacional de Colombia

February 26, 2024

## Abstract

This work investigates observations of gradual upward phase shifting of temperature oscillations in a steep tropical reservoir, which differ from the  $\pi$  radians sharp shifts that are usually accepted for the description of baroclinic motions in terms of normal modes. Supported on numerical modeling and theoretical inviscid wave ray tracing, we show that the gradual upward phase shifting is the signature of vertically propagating seiches, which refer to basin-scale oscillations that are stationary in the horizontal but propagate downwards in the vertical. We show that the vertically propagating seiche occurs due to the predominant supercritical reflection of the internal wave rays at the lake boundaries, which focuses the internal wave energy downwards with a minor fraction of the energy reflected upwards, resulting in a net downward energy propagation. The net downward energy flux precludes the formation of standing waves, with potential implications for the common framework of the energy flux path at the interior of stratified lakes. The analysis supports that vertically propagating seiches and standing mode preclusion are expected to occur in any given lake, but their signatures are more evident in steep sided lakes, with a wide metalimnion and/or for lower forcing frequencies, characteristic of higher order vertical modes.

1

2 VERTICALLY PROPAGATING SEICHES AND STANDING MODES PRECLUSION  
3 IN A STEEP-BOTTOM TROPICAL RESERVOIR

4

5 Andrés Posada-Bedoya<sup>1</sup>, Andrés Gómez-Giraldo<sup>2</sup>, Ricardo Román-Botero<sup>3</sup>

6

7 DRAFT

8 February 2024

9

10 Running head: Vertically propagating seiches

11

12 <sup>1,2,3</sup>Department of Geosciences and Environment, Universidad Nacional de Colombia, Calle  
13 59A No 63-20, Medellín, Colombia.

14 <sup>1</sup>Now at Department of Civil Engineering, Queen's University, Kingston, Ontario, ON K7L  
15 3N6, Canada

16 <sup>1</sup>Corresponding author. Email: 21afpb@queensu.ca

17 <sup>2</sup>Email: eagomezgi@unal.edu.co

18 <sup>3</sup>Email: rroman@unal.edu.co

19 Keywords: vertical propagation, standing waves, supercritical reflection, steep lake

20 **Abstract**

21 This work investigates observations of gradual upward phase shifting of temperature  
22 oscillations in a steep tropical reservoir, which differ from the  $\pi$  radians sharp shifts that are  
23 usually accepted for the description of baroclinic motions in terms of normal modes.  
24 Supported on numerical modeling and theoretical inviscid wave ray tracing, we show that  
25 the gradual upward phase shifting is the signature of vertically propagating seiches, which  
26 refer to basin-scale oscillations that are stationary in the horizontal but propagate downwards  
27 in the vertical. We show that the vertically propagating seiche occurs due to the predominant  
28 supercritical reflection of the internal wave rays at the lake boundaries, which focuses the  
29 internal wave energy downwards with a minor fraction of the energy reflected upwards,  
30 resulting in a net downward energy propagation. The net downward energy flux precludes  
31 the formation of standing waves, with potential implications for the common framework of  
32 the energy flux path at the interior of stratified lakes. The analysis supports that vertically  
33 propagating seiches and standing mode preclusion are expected to occur in any given lake,  
34 but their signatures are more evident in steep sided lakes, with a wide metalimnion and/or  
35 for lower forcing frequencies, characteristic of higher order vertical modes.

36

37 **Plain Language Summary**

38 In stratified lakes, large scale perturbations like those generated by the wind propagate as  
39 internal waves, with oscillatory motions of the particles that propagate in trajectories forming  
40 an angle with the horizontal. When they bounce at the lake contour, change direction but  
41 keep the angle of propagation respect to the horizontal plane. Incident and reflected waves

42 superpose and, under the ideal condition of no energy losses, form stationary basin scale  
43 internal waves, with points where there are no oscillations of the particles, which are called  
44 nodes. Although there is some energy loss along the propagation of the waves, in several  
45 cases they are small and natural mode theory describes the reality closely, so it is common  
46 to describe basin-scale periodic motions in terms of standing waves. We investigated  
47 observations of oscillatory basin-scale motions in a steep-sided tropical reservoir that are not  
48 stationary but have nodes that propagate upwards, which is a signature of wave energy  
49 propagating downwards. We show that this is the result of the reservoir sides being steeper  
50 than the trajectories of propagation of the waves, leading to accumulation of energy in the  
51 lake bottom instead of a reflection that allows for stationary waves to form.

52

### 53 **Key points**

- 54 • Net downward internal wave energy flux can occur in stratified lakes due to the  
55 imperfect reflection of internal wave rays.
- 56 • Predominant supercritical reflection of the internal wave rays at the lake boundaries  
57 results in a net downward energy propagation.
- 58 • Net downward energy propagation is more evident in steep lakes, lakes with a wide  
59 metalimnion and/or at lower forcing frequencies.

## 60 **1. Introduction**

61 The classical interpretation of coherent basin-scale internal motions in stratified lakes and  
62 reservoirs has been based on the decomposition onto its natural non-dissipative oscillation  
63 modes. This approach has been useful to understand the complex field of baroclinic motions  
64 at the basin scale and their energy flux path through the interactions of modes with the  
65 topography (Kocsis et al. 1998; Vidal et al. 2013), between modes (de la Fuente et al. 2008,  
66 2010), with the bottom boundary layer (Lemckert et al. 2004; Simpson et al. 2011) and with  
67 the turbulent field (Boegman et al. 2003; Gómez-Giraldo et al. 2008; Ulloa et al. 2015), which  
68 finally impact water quality through mixing and transport (Evans et al. 2008; Pernica et al.  
69 2013).

70 Strictly speaking, pure non-dissipative modes do not exist in real sloping bottom lakes  
71 (Shimizu and Imberger 2008) because the irregular bathymetry creates some residual  
72 unbalance between focusing and defocusing of some wave rays so they do not close upon  
73 themselves (Maas and Lam 1995; Thorpe 1998). Focusing of wave rays also concentrates  
74 energy and enhances viscous dissipation so the reflected rays have less energy than the  
75 incident rays, resulting in some degree of energy net downward propagation as upward and  
76 downward propagating rays do not have the same energy. In some cases, the energy net  
77 vertical flux is negligible, and the internal mode approach leads to good agreement with  
78 observations (Shimizu and Imberger 2008; Imam et al. 2013), while in other cases such  
79 approach is unable to approximate some characteristics of the oscillatory internal motions  
80 (Henderson and Deemer 2012). For instance, the internal mode approach predicts sharp  
81 changes of phase through the water column, while gradual changes of phase have been  
82 observed in several reservoirs (Lazerte 1980; Vidal and Casamitjana 2008; Henderson 2016).

83 Therefore, it is very pertinent to understand when the classical description of the oscillatory  
84 motions in terms of modes is inappropriate and should be precluded, and what else is  
85 necessary to better understand and describe the energy flux path at the interior of lakes  
86 (Imberger 1998; Wüest and Lorke 2003).

87 The bulk of research on baroclinic oscillations has focused on natural mild slope lakes, with  
88 predominant subcritical slopes, where most of the downward propagating energy introduced  
89 by the wind is reflected upwards at the bottom, allowing for standing waves formation. In  
90 those cases, the internal wave field can be well described in terms of the non-dissipative  
91 modes and perfect reflections can be considered. Conversely, in steep bottoms systems,  
92 slopes may be mostly supercritical and focus wave energy downwards upon reflection,  
93 reducing the upward wave energy available for the interference necessary to produce  
94 standing modes, so the resulting basin-scale oscillations after superposition are stationary in  
95 the horizontal but propagate downwards in the vertical, and standing waves do not develop,  
96 as first hypothesized by Thorpe (1998) and evidenced by Henderson and Deemer (2012).  
97 Following Henderson and Deemer (2012) and Henderson (2016), we call them vertically  
98 propagating seiches. In such a case, an upward phase shifting with depth of the temperature  
99 and velocity fluctuations is a clear signature of downward energy flux (Henderson and  
100 Deemer 2012). As steep lakes have been far less studied, the robustness of the non-dissipative  
101 mode model has not been thoroughly explored, so it is important to investigate conditions for  
102 its preclusion and identify the characteristics of the vertically propagating seiches when the  
103 mode is not formed.

104 This work is motivated by observations and numerical modeling in a steep reservoir that  
105 showed a coherent gradual vertical shifting in the phase of horizontal mode one basin-scale

106 oscillations with depth, very different from the  $\pi$  radians sharp shifts that are usually accepted  
107 for the description of baroclinic motions in terms of normal modes. Supported on numerical  
108 modeling and theoretical tracing of wave rays, we identify these motions as vertically  
109 propagating net oscillations, produced by the superposition of downward propagating waves  
110 and upward propagating reflected waves which are less energetic due to the dominant  
111 supercritical reflection of internal waves at the lake sloping bottom. We discuss the role of  
112 the sloping bottom on the standing mode preclusion and provide some context of our results  
113 respect to other lakes, supported on previously proposed parameterizations.

114

## 115 **2. Theoretical background**

116 Inviscid internal waves in a stratified fluid can be seen as a set of rays, whose energy  
117 propagates at an angle  $\theta$  respect to the horizontal, depending on the background stratification,  
118 characterized by the buoyancy frequency  $N$ , and wave frequency  $\omega$ :

$$\sin \theta = \frac{\omega}{N} \quad (1)$$

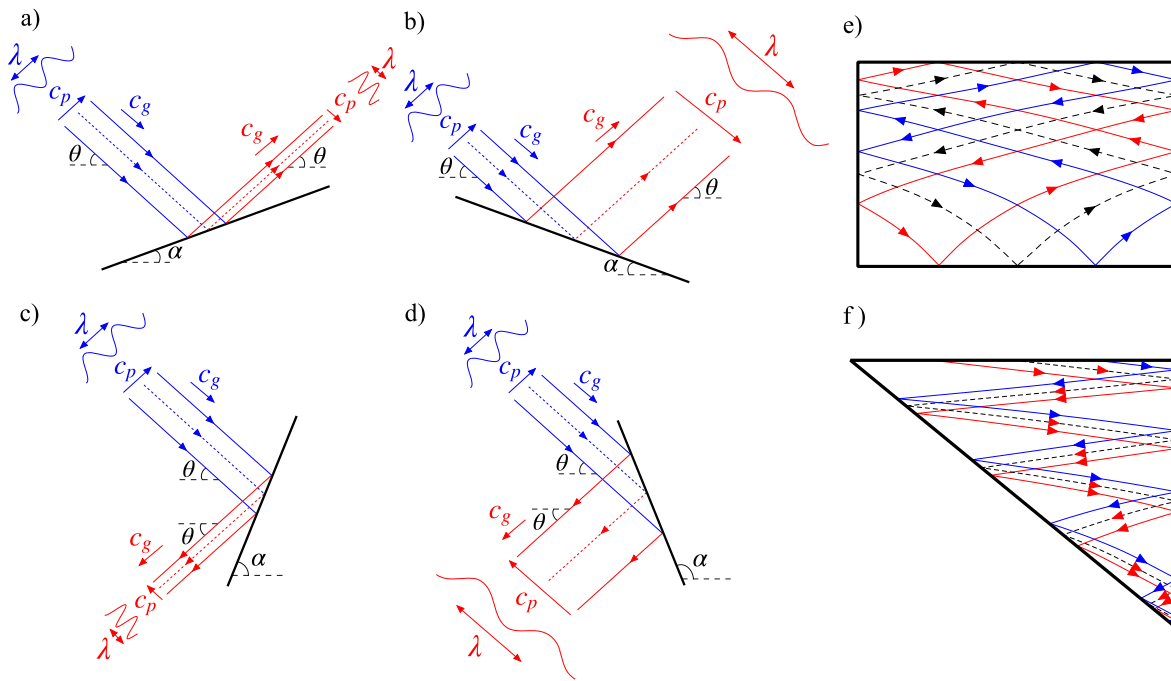
119 The fluid particle velocity  $\vec{u}$  is orthogonal to the phase velocity  $\vec{c}_p = \omega/\vec{k}$ , where  $\vec{k}$  is the  
120 wavenumber vector. The direction of energy propagation coincides with the direction of the  
121 particle motions, so the group velocity  $\vec{c}_g$  and  $\vec{c}_p$  are orthogonal with opposite vertical  
122 components (Turner 1973), such that downward (upward) wave energy flux is accompanied  
123 by upward (downward) phase propagation (Figure 1).

124 Internal wave rays maintain their propagating angle with the horizontal plane ( $\theta$ ) upon  
125 reflection at a solid boundary (Maas and Lam 1995), so incident and reflected rays make  
126 different angles to the sloping bottom, leading to wavelength change upon reflection (Fig. 1).

127 A decrease in wavelength after reflection is known as focusing (Fig. 1a, c) and a increase as  
128 defocusing (Fig. 1b, d). When the bottom slope  $\alpha$  is milder than that of the ray ( $\alpha < \theta$ ), the  
129 reflection is subcritical and the ray shifts its vertical direction of propagation upon reflection,  
130 so downward propagating waves are reflected upwards (Fig. 1a, b). If the boundary slope is  
131 steeper than the ray ( $\alpha > \theta$ ), downward propagating rays continue traveling downwards  
132 upon reflection (Fig. 1c, d). When wave energy propagation and bottom slopes are similar,  
133 i.e. close to the critical condition, large wave energy concentration (focusing) leads to a large  
134 amplitude reflected wave which turns into turbulence by overturning instability (Dauxois et  
135 al. 2004), with large wave energy loss, so the reflected wave is far less energetic than the  
136 incident one.

137 Standing waves occur when opposite identical progressive waves interfere. Because of the  
138 inclined paths of individual wave rays in stratified flows (eq. 1), the condition for standing  
139 modes to form is that every wave ray closes upon itself after bouncing from the boundaries  
140 (Fig. 1e) (Cushman-Roisin et al. 1989; Maas and Lam 1995). Moreover, because of the  
141 irregular bottom in natural basins, for a given forcing frequency there are always some rays  
142 that do not close upon themselves, so standing wave excitation is not perfect, and some  
143 degree of energy downward propagation always remains. Also, viscous dissipation and  
144 transference to turbulence reduces energy in the waves as they travel through the basin and  
145 bounce at the boundaries, so the upward reflected waves are less energetic, and upon  
146 interference with the downward waves, a residual downward propagation remains. These  
147 energy losses are small in mild slope natural lakes with significant subcritical reflection  
148 (Wiegand and Chamberlain 1987; Münnich et al. 1992; Imam et al. 2013). In some cases,  
149 most of the wave rays can be trapped by successive reflections at the boundaries towards

150 particular regions of the basin, like the shore or the bottom, and no longer close upon  
 151 themselves, precluding standing waves (Thorpe 1998). In particular, when supercritical  
 152 reflection is dominant, wave rays are focused towards the bottom and a minor fraction of  
 153 energy is reflected upwards to conform the standing wave such that downward propagating  
 154 waves dominate because of the difference in downward and upward energy fluxes (Fig. 1f)  
 155 (Henderson and Deemer 2012).



156  
 157 **Figure 1.** Schematic of wave rays reflecting at a (a, b) subcritical and (c, d) supercritical solid  
 158 boundary (a, c) focusing and (b, d) defocusing. Blue and red lines denote the lines of constant  
 159 phase of incident and reflected waves respectively and arrows indicate the direction of energy  
 160 propagation. Dashed and continuous lines indicate trough and peaks of the wave respectively.  
 161 Schematic of wave ray paths for (e) a standing mode (every wave ray closes upon itself) and  
 162 (f) vertically propagating seiche in a supercritical basin (wave rays are trapped at the bottom).  
 163

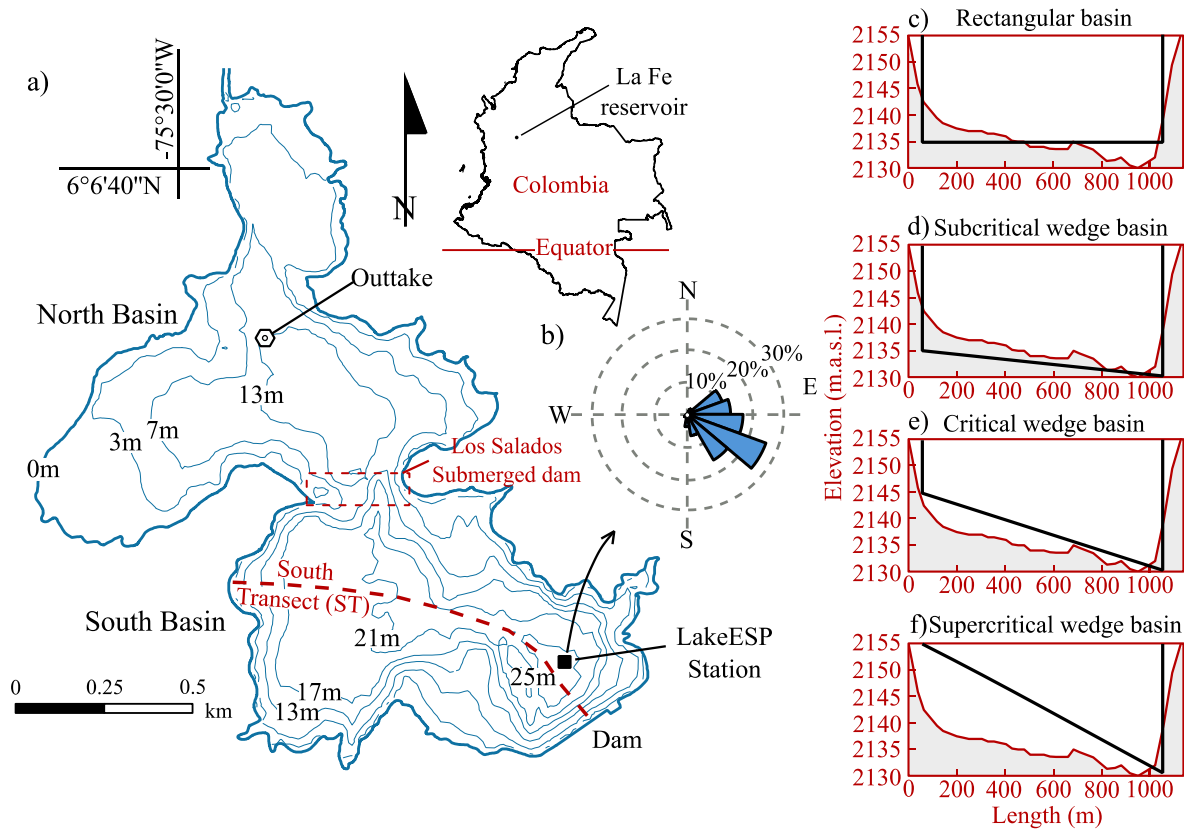
164 **3. Materials and methods**

165 3.1. Study site and field measurements

166 La Fe is a tropical reservoir located in the Northwest of Colombia (06°06'40"N,  
167 75°30'00"W) at 2150 m.a.s.l. on the Andean Mountain range (Fig. 2). This tropical Andean  
168 reservoir remains thermally stratified through the year, with seasonal changes ruled by the  
169 inflow discharge (Román-Botero et al. 2013; Posada-Bedoya et al. 2021; Posada-Bedoya et  
170 al. 2022). The reservoir is composed of two basins (North and South) separated by a shallow  
171 and narrow neck formed by the old-submerged dam Los Salados.

172 After Posada-Bedoya et al. (2022) showed that internal oscillations in each basin are  
173 decoupled, we will focus here on the South basin, where a LakeESP platform equipped with  
174 a thermistor chain and a meteorological station was installed close to the dam site (Fig. 2) to  
175 collect data every 5 min from 6 to 22 September 2012. Thirteen temperature loggers were  
176 hanging from the float at depths of 0.7, 1.5, 2.3, 3.0, 3.8, 4.5, 5.3, 6.1, 7.3, 9.1, 11.2, 13.2,  
177 15.2 m, and one additional thermistor was moored 1 m above the lake bottom. Temperature  
178 loggers had a resolution of 0.0001°C and an accuracy of 0.01°C. The meteorological station  
179 measured air temperature, atmospheric pressure, relative humidity, net shortwave and  
180 longwave radiation, rainfall, and wind speed and direction.

181 The periodic wind excites 24, 12 and 6-h basin-scale horizontal mode 1 oscillations in the  
182 South basin that are decoupled and have different vertical structure in both basins of the  
183 reservoir (Posada-Bedoya et al. 2022). The more energetic mode shows a vertical structure  
184 that resembles that of a stationary vertical mode 4, so it could be classified as a V4H1 mode.  
185 However, sharp phase changes between layers, as are predicted by normal modes, were not  
186 observed and a coherent gradual shift with depth in the phase was observed instead.



187

188 **Figure 2.** (a) Location and bathymetry of La Fe reservoir and LakeESP station location. (b)  
 189 Wind rose for wind speeds faster than  $2.5 \text{ m s}^{-1}$ . (c-f) Bottom elevation along the South  
 190 transect shown in (a) (red line) and wedge basins for numerical experiments (black line).

191

### 192 3.2. Hydrodynamic modeling

193 Numerical experiments with the 3D hydrodynamic model AEM3D were conducted to  
 194 understand the nature of the diurnal oscillations in La Fe South basin, and to explore the  
 195 effect of the sloping bottom.

196

197 *3.2.1. AEM3D model*

198 The Aquatic Ecosystem Model (AEM3D) (Hodges and Dallimore 2016) solves the three-  
199 dimensional (3D), hydrostatic, Boussinesq, Reynolds-averaged Navier-Stokes equations, and  
200 scalar transport equations in a z-coordinate system, using a finite-difference discretization of  
201 momentum and a finite-volume discretization of conservation of mass (Hodges 2000;  
202 Hodges and Dallimore 2016). The free surface evolution is modeled implicitly, while  
203 advection of momentum and scalars are solved explicitly with an Euler-Lagrangian scheme  
204 and an ULTIMATE-QUICKEST scheme, respectively (Hodges 2000; Hodges and Dallimore  
205 2016). The model uses UNESCO (1981) equation of state to relate temperature and density.  
206 The mixed-layer algorithm computes vertical mixing throughout the water column based on  
207 an integral model of the turbulent kinetic energy equation (Hodges 2000). Horizontal mixing  
208 is solved through an eddy viscosity model. No-slip and zero normal flow boundary conditions  
209 are imposed at bottom and lateral boundary cells. Because of the staircase representation of  
210 the bottom, the model slightly overestimates numerical diffusion and internal wave damping  
211 (Gómez-Giraldo et al. 2006; Vidal et al. 2013), despite which it has been demonstrated to  
212 accurately predict basin-scale internal waves in a wide variety of lakes and reservoirs  
213 worldwide (Vidal et al. 2013; Woodward et al. 2017; Dissanayake et al. 2019).

214

215 *3.2.2. Numerical experiments*

216 After calibration of the AEM3D model with temperature records from a thermistor chain  
217 (Posada-Bedoya et al. 2021), we conducted five two-dimensional numerical experiments:  
218 one for a basin with the bottom profile of the decoupled South basin (South Transect in Fig.  
219 1) and the other four for idealized vertical walls wedge-shaped basins with different bottom

220 slopes (Fig. 2c-f). To simulate 2D basin geometries with the 3D model, we setup the  
221 bathymetry of each scenario in the  $x$ - $z$  plane (Fig. 2c-f), with an individual cell in the  
222 spanwise direction and a free-slip boundary condition on the sidewalls. Results were  
223 insensitive to the spanwise cell size.

224 For each scenario, the domain was discretized using a uniform horizontal grid of 25 m and  
225 0.4 m uniform thick layers (Table 1). We verified grid independency of the results at this  
226 spatial resolution. The time step was 10 s to meet the numerical stability condition for the  
227 internal motions. We simulated the response in each case to the forcing of an idealized wind  
228 with a speed  $v = v_0 \cos(\omega t)$ , with  $v_0 = 3 \text{ m s}^{-1}$  and a frequency  $\omega = 7.27 \times 10^{-5} \text{ s}^{-1}$  (24 h  
229 period) in the case with the shape of the South basin, as it was the period of the dominant  
230 oscillations observed in the field (Posada-Bedoya et al. 2022). For the idealized wedge  
231 basins, the forcing period was 20 h, which is the period of the theoretical V4H1 mode of the  
232 rectangular basin, according to Gill (1982) eigenmodel for the average stratification of the  
233 survey (Fig. 3b). We ran the model without other external forcing, i.e. with no other  
234 meteorological inputs than the wind, inflows, or outflows. By simulating the basins with a  
235 perfectly periodic wind forcing, we are considering the most favorable condition for the  
236 standing mode excitation in each case. The model ran for 9 days, enough time for the  
237 excitation of a standing wave, before mixing modifies the background stratification and the  
238 natural modes characteristics. The model was initialized with the average stratification of the  
239 survey (Fig. 3b), with horizontally homogeneous layers and zero velocity everywhere. The  
240 simulations were carried out using default model parameters, which were based on non-site-  
241 specific literature values (Hodges and Dallimore 2013), as in other modelling studies  
242 (Woodward et al. 2017).

243 Based on the forcing period of the idealized wedge scenarios and the minimum value of the  
 244 buoyancy frequency ( $N_{min}=0.0057$  Hz) (Fig. 3b), the critical slope ( $\theta_c = 2\pi\omega/N_{min}$ ) was  
 245 0.0153 rad, on which we relied to define the bottom slope of the wedges ( $\alpha$ ) as subcritical  
 246 ( $\alpha < 0.7\theta_c$ ), critical ( $0.7\theta_c < \alpha < 1.5\theta_c$ ) and supercritical ( $\alpha > 1.5\theta_c$ ), similar to what was  
 247 used in previous studies (Gómez-Giraldo et al. 2006; Henderson and Deemer 2012) (Table  
 248 1).

249 **Table 1.** Parameters for the setup of numerical experiments.

Scenario	$\alpha$ (rad)	$\alpha/\theta_c$	Maximum depth $H$ (m)	Length $L$ at $H/2$ depth (m)
Rectangular	0.000	0.00	20	1000
Subcritical	0.005	0.33	25	1000
Critical	0.015	0.98	25	850
Supercritical	0.025	1.63	25	500
South basin	----	----	27	1100

250

### 251 3.2.3. Analysis of model results

252 The vertical structure of the oscillations was identified from calculations of wavelet  
 253 coherence and phase (Grinsted et al. 2004) for series of temperature profiles close to the  
 254 deepest edge of the basin, and by band-pass filtering the time series of horizontal velocity  
 255 profiles predicted by the 3-D model using a fourth-order Butterworth filter.

256

### 257 3.3. Wave ray tracing

258 For each scenario, we traced the path in the time-depth ( $t-z$ ) space of constant phase lines of  
 259 linear shallow water progressive WKB waves (Phillips 1977). At a fixed horizontal position,  
 260 wave crests move vertically at speed  $c_z = \omega/k_z$  (Sutherland 2010), so constant phase lines  
 261 paths are given by

$$\frac{dz}{dt} = c_z = \frac{2\pi\omega^2\lambda_x}{N(z)} \quad (5)$$

262 where  $\lambda_x$  is the horizontal wavelength and  $k_z$  is the vertical component of the wavenumber  
 263 vector. We traced constant phase lines every  $T/2$  by solving eq. 5 at discrete time steps,  
 264 starting at the bottom in the center of the basin. We compared the path of constant phase lines  
 265 to the time-depth structure of the band-passed simulated horizontal velocity, accepting that a  
 266 close agreement indicates vertical propagation Henderson and Deemer (2012). In all the  
 267 wedge cases, the stratification and forcing frequency were the same, thus the differences in  
 268 the paths were only due to the selected wavelength  $\lambda_x$ , in this case  $2L$ , as the basin-scale  
 269 waves observed in the lake are horizontal-one (Posada-Bedoya et al. 2022), and  $L$  being the  
 270 length of the basin at the middle depth (Table 1). The path of wave ray energy in the length-  
 271 depth ( $x$ - $z$ ) space of each basin for the given forcing frequency was calculated from:

$$\frac{dz}{dx} = \tan \theta \quad (6)$$

272 Differences in wave energy paths in the wedge basins were only due to the basin geometry,  
 273 which determines the distance traveled by wave rays at different depths as they repeatedly  
 274 cross the lake and reflect from end walls while propagating from surface to bed (or from bed  
 275 to surface). Energy wave packet was not traced in the south basin because the wave ray  
 276 propagation occurs in a three-dimensional space.

277

### 278 3.4. Reflection coefficient

279 The reflection coefficient is the fraction of incident wave energy that is reflected at the lake  
 280 bottom (Henderson and Deemer 2012; Henderson 2016). The closer it is to one, the closer

281 the superposition of down and upward propagating waves is to a standing wave or natural  
 282 mode. In this work, it was calculated for each numerical experiment by adjusting the  
 283 theoretical interference pattern between downward (incident) and upward (reflected)  
 284 progressive waves to that of the modeling results. We estimated vertical profiles of power  
 285 and phase  $\hat{\psi}_M(z, \omega_0)$  of the internal wave forced at frequency  $\omega_0$  in AEM3D by computing  
 286 the Fourier transform  $\hat{\psi}_M(z, \omega)$  of the horizontal velocity signal  $u_M(z, t)$ , simulated at  
 287 several heights ( $z$ ) in the center of the basin:

$$u_M(z, t) = \sum_{\omega} \hat{\psi}_M(z, \omega) e^{i2\pi\omega t} \quad (2)$$

288 The theoretical profile of power and phase  $\hat{\psi}_T(z, \omega_0)$  for the wave forced at the frequency  
 289  $\omega_0$  was estimated as in Henderson (2016):

$$\hat{\psi}_T(z, \omega_0) = \left( \frac{N(z)}{N_0} \right)^{1/2} \hat{\psi}_{z_0} [e^{-i\phi_T(z, \omega_0)} + R e^{i\phi_T(z, \omega_0)}] \quad (3)$$

290 where  $R$  is the reflection coefficient,  $\hat{\psi}_{z_0}$  is the complex amplitude of downward-propagating  
 291 waves at the height of reference  $z_0$ ,  $N_0 = N(z_0)$ , and the theoretical phase between  $\hat{\psi}_{z_0}$  (at  
 292  $z_0$ ) and  $\hat{\psi}_T(z, \omega_0)$  at elevation  $z$  is:

$$\phi_T(z, \omega_0) = \int_{z'=z_0}^z \frac{2\pi}{\lambda_z} dz' = \int_{z'=z_0}^z \frac{N(z')}{\omega_0 \lambda_x} dz' \quad (4)$$

293 where  $\lambda_x$  and  $\lambda_z$  are the horizontal and vertical projections of the wavelength respectively.  
 294 We adjusted simultaneously  $R$ ,  $\lambda_x$  and  $\hat{\psi}_{z_0}$  by minimizing the squared error between  
 295  $\hat{\psi}_T(z, \omega_0)$  and  $\hat{\psi}_M(z, \omega_0)$  profiles, for  $\omega_0$  associated to the forcing period in each case. We  
 296 used AEM3D results above 15 m deep in the center of the basin, as below that depth the wave  
 297 rays are nearly vertical because of the reduced stratification (Fig. 3b), so the vertical

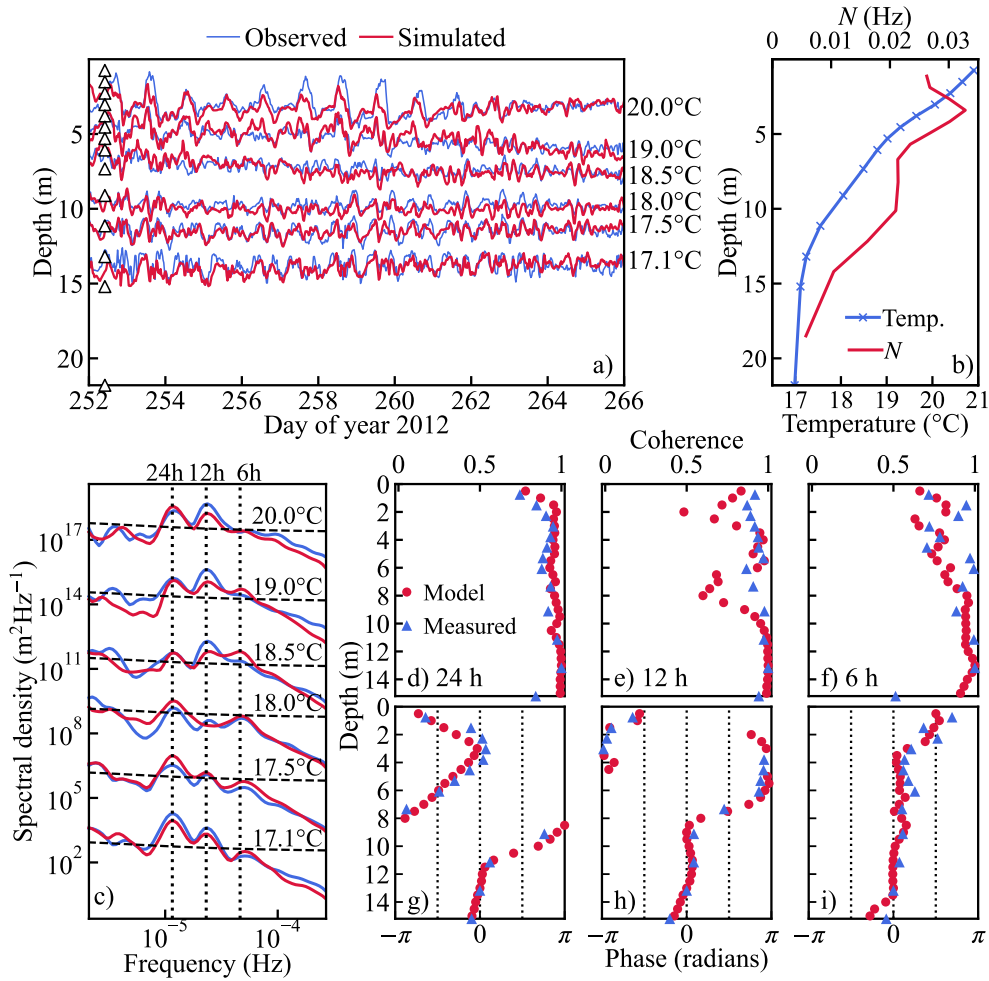
298 wavelength grows exponentially (eq. 4) and the energy profile is roughly uniform, similarly  
299 to Henderson (2016).

300

## 301 **4. Results**

### 302 4.1. Overview of field and model results

303 The background temperature vertical structure did not change significantly throughout the  
304 survey (Fig. 3a) and had a relevant gradient from the near surface down to ~14 m deep, and  
305 was nearly uniform below that depth (Fig. 3b). The wind speed exhibited a strong diel  
306 variability with the strongest winds coming from the East-Southeast (Fig. 1b) early in every  
307 afternoon and forcing internal waves with dominant periods of 24, 12 and 6 h in the South  
308 basin (Fig. 3c) oscillating along the east-west transect and being decoupled from those in the  
309 North basin (Posada-Bedoya et al. 2022). The 24-h oscillations exhibited a continuous phase  
310 shifting with depth in the top 15 m, gradually reversing direction (changing phase by  $\pi/2$   
311 radians) three times in both field and model results (Fig. 3d, g), which is indicative of vertical  
312 propagation of wave energy. The internal waves of 12-h and 6-h period exhibited structures  
313 resembling V2 (Fig. 3e, h) and V1 (Fig. 3f, i) oscillations.



314

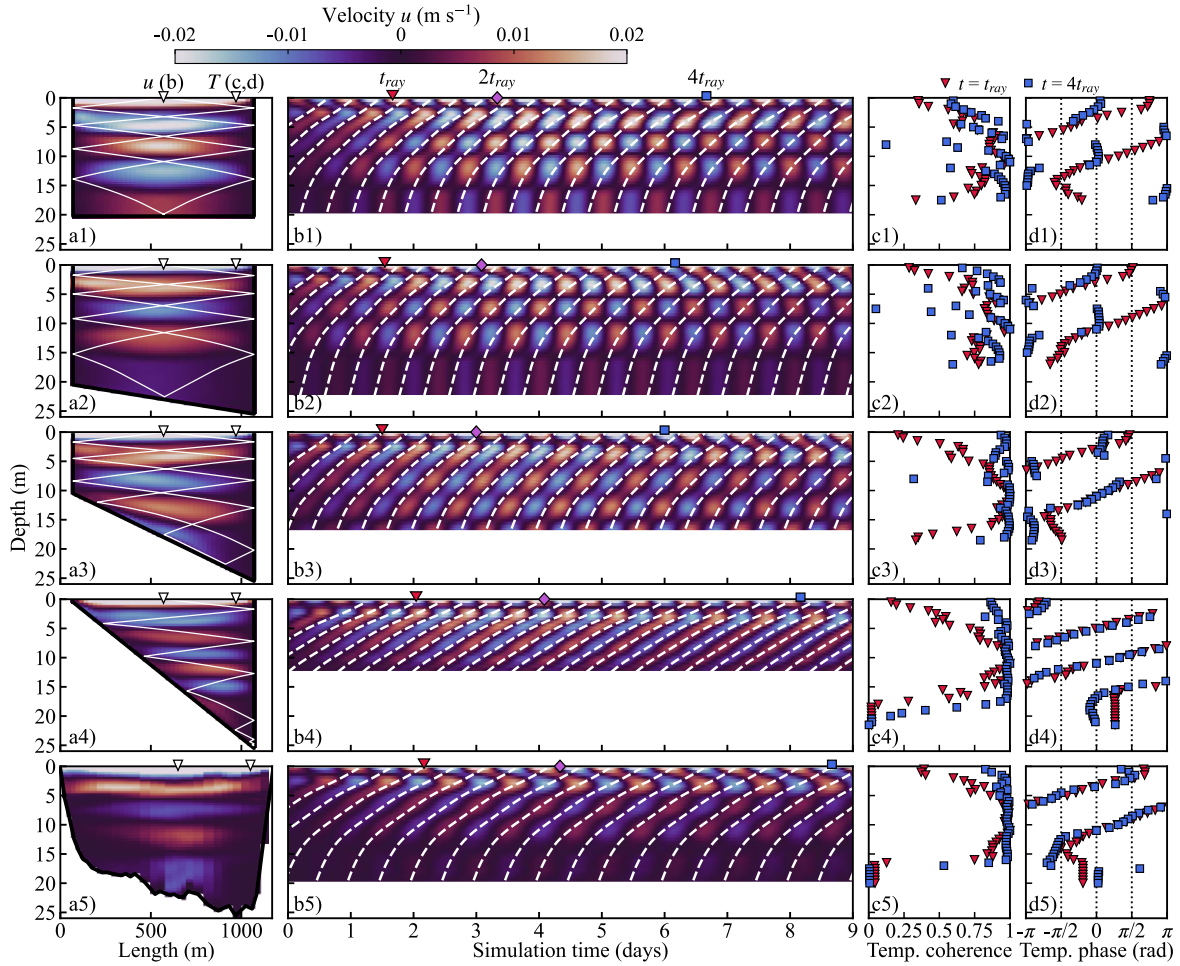
315 **Figure 3.** (a) Isotherm depths estimated from measurements and model results. The triangles  
 316 indicate the depth of the thermistors. (b) Average temperature and buoyancy frequency  
 317 profiles. (c) Global wavelet spectra of the observed (blue lines) and modeled (red lines)  
 318 isotherm displacements. Dashed line indicates the threshold for significant energy with a  
 319 95% confidence. Offset between spectra is three logarithmic cycles. Profiles of wavelet (d,  
 320 e, f) coherence and (g, h, i) phase of the temperature fluctuations of (d, g) 24 h, (e, h) 12 h  
 321 and (f, i) 6 h period oscillations. Coherence and phase are relative to the 13 m deep  
 322 temperature signal.

323

## 324 4.2. Periodically wind-forced basins

325 We define  $2t_{ray}$  as the time required for wave energy to travel downwards from the surface,  
326 bounce at the bottom and return to the surface. In all the scenarios, before a time  $\sim 2t_{ray}$ ,  
327 the phase profile of temperature oscillations exhibited a continuous upward shifting (Fig. 4d),  
328 indicating that before a time  $\sim 2t_{ray}$  the wave energy fluxed downwards as in a progressive  
329 wave, excited by the first cycle of wind forcing. Unlike vertically standing modes, the band-  
330 passed horizontal velocity in the time-depth space showed upward phase propagation  
331 matching the theoretical upward propagation of constant phase lines (Fig. 4b).

332 In the rectangular and subcritical basins, from a time  $\sim 2t_{ray}$  onwards the horizontal velocity  
333 in the time-depth space exhibited the arrangement of oscillating cells, characteristic of a  
334 standing mode (Fig. 4b1, b2 and Supplementary Videos 1 and 2). The coherence of  
335 temperature oscillations decreased at depths where phase shifts close to  $\pi$  radians occurred,  
336 suggesting the presence of nodes of vertical displacements in a standing wave (Fig. 4 c1, c2,  
337 d1, d2). The ray tracing predicted wave rays closing upon themselves for wave periods of  
338 19.4 and 18.9 h for rectangular and subcritical cases respectively (Fig. 4a1, a2), after  
339 bouncing four times at each lateral wall, in agreement with the estimated V4H1 mode of 20-  
340 h period of the rectangular basin.



341

342 **Figure 4.** (a) Depth-length curtain of band-passed horizontal velocity at a time of maximum  
 343 kinetic energy. Panels 1-5 are respectively for rectangular, subcritical, critical, supercritical  
 344 and South basins. The white line in panels a1-a4 is the path of an energy wavepacket excited  
 345 at the center of the lake surface. (b) Time-depth contours of the band-passed horizontal  
 346 velocity in the center of the basin. White dashed lines show the path of theoretical constant  
 347 phase lines. Profiles of (c) coherence and (d) phase of temperature oscillations at the deepest  
 348 part of the basins (location indicated in panels a), at the times indicated by markers in panels  
 349 (b). Coherence and phase are relative to the 10 m deep temperature signal.

350

351 In the supercritical case the horizontal velocity structure in the time-depth space showed  
352 upward phase propagation consistent with the theoretical constant phase lines of progressive  
353 waves for the entire simulation (Fig. 4b4 and Supplementary Video 4). The coherence of  
354 temperature oscillations was high throughout the water column (Fig. 4c4), so nodes and  
355 antinodes characteristic of a standing wave did not occur, contrasting with the nodes and  
356 antinodes observed in the rectangular and subcritical cases. The continuous upward phase  
357 shifting remained throughout the simulation very similar to that before  $2t_{ray}$  (Fig. 4d4),  
358 suggesting a permanent downward propagation of energy and that standing modes of 20-h  
359 period were not formed, despite the ideal periodic forcing conditions for their excitation. The  
360 ray tracing in the  $x$ - $z$  space showed the continuous downward reflection at the boundaries  
361 and the consequent trapping of the wave energy at the bottom of the basin for waves of 20 h  
362 period (Fig. 4a4). The oscillations had a vertical structure higher than V4, due to the increase  
363 in the number of times the ray crosses the lake from side to side (Fig. 4a4), as the vertical  
364 wavelength ( $\lambda_z = 4\pi\omega L/N$ ) is shorter because of the smaller  $L$ .

365 The nearly critical case was a transitional condition between subcritical and supercritical  
366 cases. The phase showed a hybrid structure with  $\sim \pi$  radians shifts at some depths and  
367 upward shifting between 7 and 14 m (Fig. 4d3 and Supplementary Video 3). The coherence  
368 reductions were less marked than in the rectangular and subcritical cases (Fig. 4c3), even  
369 after several cycles of wind forcing, so nodes were not clearly developed. The wave ray  
370 closed upon itself for a period of 20.2 h, but propagated nearly parallel to the sloping bottom  
371 after reflection (Fig. 4a3), so the inviscid ray tracing is expected to be invalid because of the  
372 large dissipation associated to the instabilities associated to the nearly critical reflection  
373 expected in this region (Dauxois et al. 2004).

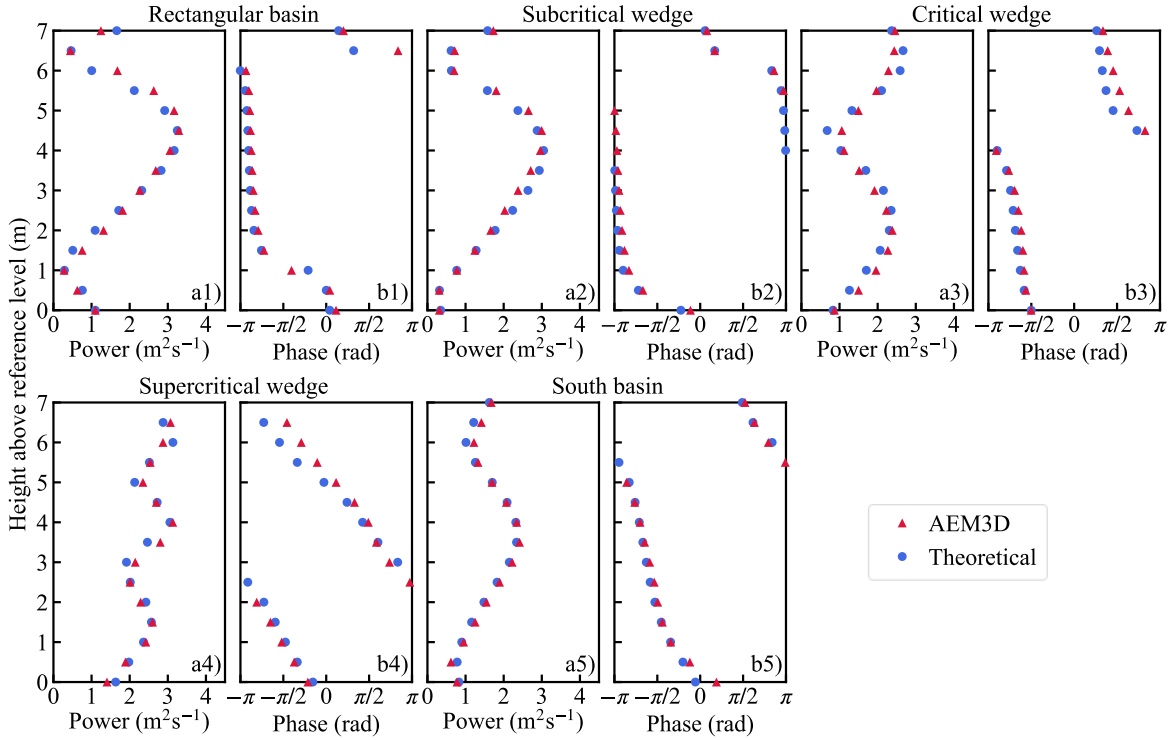
374 In the south basin experiment, as in the supercritical case, the horizontal velocity structure in  
375 the time-depth space did not develop the cell structure associated to standing modes, and  
376 instead, it kept the progressive wave signature, fitting the theoretical phase of progressive  
377 waves throughout the simulation (Fig. 4b5 and Supplementary Video 5). The phase structure  
378 of temperature oscillations maintained a gradual upward shifting (Fig. 4d5) like the one  
379 obtained from field measurements and the 3D simulation (Fig. 3g). Coherence was high  
380 throughout the water column, indicating nodes and antinodes did not occur (Fig. 4c5).  
381 According to this, despite the ideal periodic wind forcing, the standing mode of 24 h period  
382 was not formed and instead a vertically propagating internal seiche was excited. A very  
383 similar result was obtained when the system was forced with a 20-h period wind (not shown).  
384 As in the field and model validation, the phase profile reverses its slope around the depth of  
385 maximum  $N$  ( $\sim 3$  m), in agreement with the relation between phase and buoyancy frequency  
386 in eq. 4.

387

#### 388 4.3. Reflection coefficient

389 The theoretical pattern of interfering progressive waves fits very well to the power and phase  
390 profiles estimated from AEM3D results (Fig. 5), so the adjusted  $R$  and  $\lambda_x$  (Table 2) are  
391 reliable. The reflection coefficient is higher for the rectangular and subcritical cases and  
392 reduces dramatically for the supercritical scenario, while the nearly critical case poses a  
393 transition between both conditions. In the real bathymetry of the south basin, the reflection  
394 coefficient was between those for the critical and supercritical cases, in accordance with the  
395 signatures of vertical propagation shown above. The adjusted  $\lambda_x$  was always very close to  
396  $2L$  (cf.  $L$  at  $H/2$  depth in Table 1 to  $\lambda_x$  in Table 2), consistent with the horizontal-one

397 oscillations. Nodes and antinodes of a standing wave can be identified in the rectangular and  
 398 subcritical cases but are less evident as the bottom slope increases and in the south basin.



399

400 **Figure 5.** Power and phase profiles estimated from AEM3D results and from theoretical  
 401 interference between opposite progressive waves.

402 **Table 2.** Fitted reflection coefficient  $R$  and horizontal wavelength  $\lambda_x$  for each scenario.

Scenario	$\alpha/\theta_c$	$R$	$\lambda_x$ (m)
Rectangular	0.00	0.89	2000
Subcritical	0.33	0.85	2187
Critical	0.98	0.62	1711
Supercritical	1.60	0.14	1037
South basin	----	0.42	2378

403

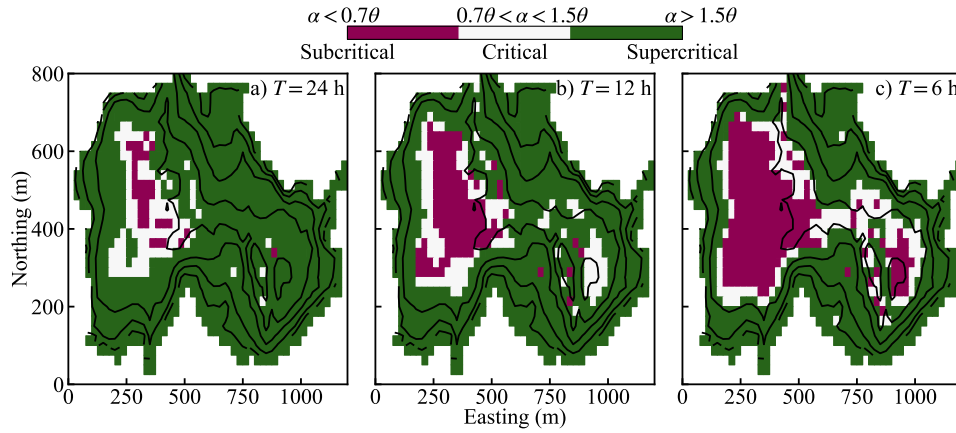
## 404 5. Discussion

### 405 5.1. Role of the sloping bottom on the vertical propagation

406 Numerical experiments indicate that diurnal standing waves were precluded in La Fe South  
407 basin and, instead, a 24-h period vertically propagating horizontal mode one seiche was  
408 observed. Comparing the slopes of the wave ray path (calculated with eq. 1 for the measured  
409 average buoyancy frequency at the bottom) and the bottom, we classified the reflection as  
410 subcritical ( $\alpha < 0.7\theta_c$ ), critical ( $0.7\theta_c < \alpha < 1.5\theta_c$ ) or supercritical ( $\alpha > 1.5\theta_c$ ) (Fig. 6a),  
411 and found that most of the reflections of 24-h period waves in the south basin are  
412 supercritical, explaining why a downward vertically propagating seiche is observed instead  
413 of a standing vertical mode. Because of the predominant supercritical reflection, internal  
414 wave energy is focused and trapped at the bottom, where it is expected to be the main source  
415 of energy for the bottom boundary layer, as in Henderson (2016), differing from the common  
416 framework of the energy flux path at the interior of stratified lakes (Imberger 1998; Wüest  
417 and Lorke 2003), with potential implications for mixing and transport processes that impact  
418 water quality.

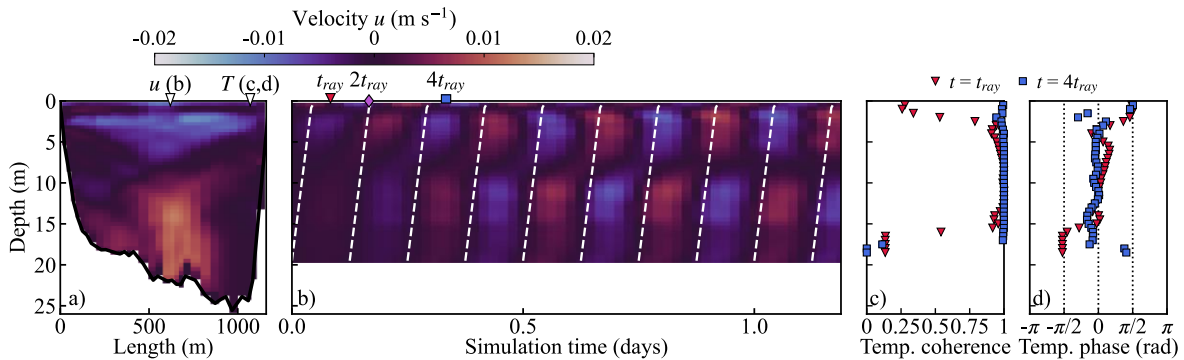
419 As the forcing frequency increases, the area where reflection is subcritical grows (Fig. 6) and  
420 more energy can be reflected upwards at the sloping bottom and standing waves can be  
421 observed. This is illustrated by forcing the south basin with 6-h period winds, which excite a  
422 coherent V1H1 response (Fig. 7) (Supplementary Video 6). Increasing supercritical  
423 reflection for lower forcing frequencies implies that higher order vertical motions are more  
424 likely to occur as vertically propagating seiches and are less suitable to be described as  
425 standing modes. This is consistent with the gradual phase shifting in the temperature and

426 velocity profiles, observed more often in lakes with dominant oscillations of high vertical  
 427 order (Lazerte 1980; Serra et al. 2007; Henderson and Deemer 2012).



428

429 **Figure 6.** Spatial classification of the sloping bottom of the South basin for wave periods of  
 430 (a) 24, (b) 12 and (c) 6 h.



431

432 **Figure 7.** Response of the South basin to a 6-h period forcing: (a) Curtain along the south  
 433 transect (ST) of band-passed horizontal velocity after one day of simulation, (b) Time-depth  
 434 contours of the band-passed horizontal velocity in the middle of the basin, with white dashed  
 435 lines showing the path of theoretical constant phase lines. (c) Coherence and (d) phase of  
 436 temperature profiles at the deepest edge of the basin (panels a) at the times indicated by  
 437 markers in panels (b).

438

## 439 5.2. Ubiquity of vertically propagating seiches

440 The reflection coefficient for the rectangular and subcritical cases was slightly lower than 1,  
441 indicating that the reflected energy was lower than the incident and a net residual downward  
442 energy propagation occurred, despite clear signatures of standing waves being identified in  
443 those cases. This shows that some degree of vertical propagation of basin-scale internal  
444 waves should always be expected, even in the simplest rectangular basin. Still, a large bulk  
445 of research has been conducted using the inviscid natural mode concept to describe basin-  
446 scale internal waves in lakes (Wiegand and Chamberlain 1987; Münnich et al. 1992; Imam  
447 et al. 2013).

448 We conjecture that vertically propagating seiches have not been widely explored because  
449 systems with adequate conditions for them to be clearly evident, like steep walls and wide  
450 metalimnion, have been far less studied. Most descriptions of basin-scale internal waves have  
451 been conducted in natural mild slope lakes, where a significant subcritical reflection occurs  
452 such that appreciable standing waves develop even if some small degree of vertical  
453 propagation remains, and in temperate systems with a thin metalimnion. In the latter case,  
454 the stratification is weak above (in the surface layer) and below (the hypolimnion) of the thin  
455 metalimnion, so wave ray paths are nearly vertical in those regions of the water column, and  
456 the phase shifting is mainly confined to within the thin metalimnion, making it difficult to  
457 distinguish the gradual phase shifting when occurring. Instead, in systems with a wide  
458 metalimnion, the signature of the gradual phase shifting with depth extends through a larger  
459 depth range, so it is more evident when occurring, as in some shallow summer temperate  
460 lakes (Lazerte 1980), temperate reservoirs with selective withdrawal at intermediate depths

461 (Serra et al. 2007), or tropical Andean reservoirs during moderate dry conditions (Posada-  
 462 Bedoya et al. 2019).

463 To provide a global context of the degree of vertical propagation in La Fe, in comparison  
 464 with other lakes, we estimated the parameters  $D = NH/(\pi\omega L)$  (Henderson and Deemer  
 465 2012) and reflection coefficient  $\mathcal{R}$  (Henderson 2016), defined in terms of readily available  
 466 variables measured in the field, for several systems where high order vertical modes were  
 467 dominant (Table 3). The parameter  $D$  is the ratio of mean lake ( $2H/L$ ) to wave ray ( $2\pi\omega/N$ )  
 468 slopes. High values of  $D$  are typical of steep and/or strongly stratified lakes, with dominant  
 469 supercritical reflection and vertical propagation, and low values are typical of mild slope  
 470 and/or weakly stratified lakes, with a dominant subcritical reflection that favors standing  
 471 waves excitation. The parameter  $\mathcal{R}$  is a parameterization of the reflection coefficient  $R$  in  
 472 terms of readily available variables measured in the field. It was estimated as (Henderson  
 473 2016):

$$\mathcal{R} = \frac{1 - \beta}{1 + \beta} \quad (8)$$

$$\beta = 2 \left( \frac{8}{\pi} \right)^{1/2} C_D \frac{v_{RMS}}{c_{gz}} \quad (9)$$

474 where  $C_D$  is the bottom drag coefficient,  $v_{RMS}$  is the root-mean-square of the velocity of the  
 475 internal waves induced currents, and  $c_{gz}$  is the vertical component of the group velocity,  
 476 with the same magnitude of the vertical phase velocity in eq. (5). A value of  $\mathcal{R} = 1$  indicates  
 477 perfect reflection. For the calculations, we assumed a typical value of  $C_D = 2 \times 10^{-3}$ , as in  
 478 Henderson (2016).

479 For all the selected cases,  $\mathcal{R} < 1$  and  $D > 1$ , illustrating some degree of vertical propagation  
480 occurred in all of them. The lowest values of  $\mathcal{R}$  coincide with the highest values of  $D$  in  
481 systems where signatures of vertically propagating seiches were identified by Henderson  
482 (2016) (Frains Lake and Sau reservoir) and where the vertical propagation was reported  
483 (Lacamas Lake and La Fe reservoir). Lake Alpnach and Wood Lake are natural lakes with  
484 nearly flat bottom and alike rectangular morphometries, so they have the highest  $\mathcal{R}$  and  $D \sim 1$ ,  
485 with signatures of appreciable standing waves in the referred articles. The analysis supports  
486 that vertically propagating basin-scale internal waves is the rule rather than the exception.

487 **Table 3.** Parameters of internal wave reflection in selected lakes. [1] Münnich et al. (1992),  
488 [2] Lazerte (1980), [3] Serra et al. (2007), [4] Wiegand and Chamberlain (1987), [5]  
489 Henderson and Deemer (2012), [6] present study.

Lake [source]	$L$ (m)	$H$ (m)	$N$ (Hz)	$T$ (h)	$v_{RMS}$ (m/s)	$D$	$\mathcal{R}$
Lake Alpnach [1]	5000	21.6	0.01	24	0.02	1.2	0.74
Frains Lake [2]	300	4	0.05	7	0.008	5.3	0.48
Sau reservoir [3]	3600	30	0.02	24	0.02	4.6	0.45
Wood Lake [4]	6800	26	0.02	24	0.02	2.1	0.80
Lacamas Lake [5]	1500	15	0.03	24	0.016	8.0	0.25 <sup>†</sup>
La Fe reservoir [6]	1000	20	0.02	20	0.01	9.2	0.41 <sup>†</sup>

490 <sup>†</sup>Directly estimated from the fit of a theoretical pattern to model or field results.

491

## 492 6. Conclusions

493 We used numerical modeling and theoretical inviscid wave ray tracing to explain  
494 observations of vertical gradual phase shifting of temperature oscillations in a steep reservoir.  
495 Due to the dominant supercritical reflection in the reservoir, 24-h period oscillations were  
496 identified as vertically propagating internal seiches, characterized by high coherence  
497 throughout the water column and gradual upward phase shifting of temperature and velocity

498 profiles, and standing waves of 24-h period did not form. For lower forcing frequencies,  
499 characteristic of higher order vertical modes, the supercritical reflection increases, so higher  
500 order vertical motions are more likely to occur as vertically propagating seiches and are less  
501 suitable to be described by standing mode theory.

502 We conclude that vertical propagating basin scale internal waves are ubiquitous to stratified  
503 lakes and reservoirs, due to the imperfect reflection of internal wave rays and viscous  
504 dissipation, whilst the non-dissipative modal description is a valid approximation in systems  
505 where subcritical reflection is significant, so the amount of upward propagating reflected  
506 energy is similar to the downward incident energy, despite some degree of vertical  
507 propagation always remains. The mechanisms described in this paper, which explain vertical  
508 propagation and standing mode preclusion, are expected to occur in any given lake, but their  
509 signatures are more evident in steep sided lakes, with a wide metalimnion and/or with a  
510 significant stratification extending through the water column. In some systems where  
511 significant supercritical reflection may be important, the modal description has been used  
512 with apparent success because the signature of vertically propagating waves is difficult to  
513 observe when there is a thin metalimnion separating well mixed epilimnion and hypolimnion.

514

## 515 **7. Acknowledgments**

516 The authors thank to Empresas Públicas de Medellín (EPM) for funding the field work and  
517 providing reservoir data.

518

519 **8. Data availability statement**

520 Software for this research is available in Hodges and Dallimore (2016) at  
521 <https://www.hydronumerics.com.au/software/aquatic-ecosystem-model-3d>. Configuration  
522 files for the simulations presented here and field data for this research will be available at a  
523 repository by the time of publication.

524

525

526 **9. References**

- 527 Boegman, L., J. Imberger, G. N. Ivey, and J. P. Antenucci. 2003. High-frequency internal  
528 waves in large stratified lakes. *Limnol. Oceanogr.* **48**: 895–919.
- 529 Cushman-Roisin, B., V. Tverberg, and E. G. Pavia. 1989. Resonance of internal waves in  
530 fjords: A finite-difference model. *J. Mar. Res.* **47**: 547–567.  
531 doi:10.1357/002224089785076190
- 532 Dauxois, T., A. Didier, and E. Falcon. 2004. Observation of near-critical reflection of internal  
533 waves in a stably stratified fluid. *Phys. Fluids* **16**: 1936–1941. doi:10.1063/1.1711814
- 534 Dissanayake, P., H. Hofmann, and F. Peeters. 2019. Comparison of results from two 3D  
535 hydrodynamic models with field data: internal seiches and horizontal currents. *Int.*  
536 *Waters* **9**: 239–260. doi:10.1080/20442041.2019.1580079
- 537 Evans, M. A., S. MacIntyre, and G. W. Kling. 2008. Internal wave effects on photosynthesis:  
538 Experiments, theory, and modeling. *Limnol. Oceanogr.* **53**: 339–353.  
539 doi:10.4319/lo.2008.53.1.0339
- 540 Gill, A. E. 1982. *Atmosphere-Ocean Dynamics*, Academic Press.
- 541 Gómez-Giraldo, A., J. Imberger, and J. P. Antenucci. 2006. Spatial structure of the dominant  
542 basin-scale internal waves in Lake Kinneret. *Limnol. Oceanogr.* **51**: 229–246.  
543 doi:10.4319/lo.2006.51.1.0229
- 544 Gómez-Giraldo, A., J. Imberger, J. P. Antenucci, and P. S. Yeates. 2008. Wind-shear-  
545 generated high-frequency internal waves as precursors to mixing in a stratified lake.  
546 *Limnol. Oceanogr.* **53**: 354–367. doi:10.4319/lo.2008.53.1.0354

547 Grinsted, A., J. C. Moore, and S. Jevrejeva. 2004. Application of the cross wavelet transform  
548 and wavelet coherence to geophysical time series. *Nonlinear Process. Geophys.* **11**:  
549 561–566. doi:10.5194/npg-11-561-2004

550 Henderson, S. M. 2016. Turbulent production in an internal wave bottom boundary layer  
551 maintained by a vertically propagating seiche. *J. Geophys. Res. Ocean.* **121**: 2481–2498.  
552 doi:10.1002/2015JC011071

553 Henderson, S. M., and B. R. Deemer. 2012. Vertical propagation of lakewide internal waves.  
554 *Geophys. Res. Lett.* **39**: n/a-n/a. doi:10.1029/2011GL050534

555 Hodges, B. R. 2000. Numerical Techniques in CWR-ELCOM (code release v. 1). CWR  
556 Manuscr. WP **1422**.

557 Hodges, B. R., and C. Dallimore. 2013. Estuary, Lake and Coastal Ocean Model: ELCOM  
558 v2. 2 science manual, Technical report, Centre for Water Research, Univ. of Western  
559 Australia.

560 Hodges, B. R., and C. Dallimore. 2016. Aquatic Ecosystem Model: AEM3D, v1. 0. User  
561 Manual, Hydronumerics, Aust. Melb.

562 Imam, Y. E., B. E. Laval, and G. a. Lawrence. 2013. The baroclinic response to wind in a  
563 small two-basin lake. *Aquat. Sci.* **75**: 213–233. doi:10.1007/s00027-012-0268-1

564 Imberger, J. 1998. Flux paths in a stratified lake : A review, p. 1–17. *In* J. Imberger [ed.],  
565 Physical Processes in lakes and oceans. Coastal and estuarine studies. V. 54. AGU.

566 Kocsis, O., B. Mathis, M. Gloor, M. Schurter, and A. Wüest. 1998. Enhanced mixing in  
567 narrows: A case study at the Mainau sill (Lake Constance). *Aquat. Sci.* **60**: 236–252.

568       doi:10.1007/s000270050039

569   de la Fuente, A., K. Shimizu, J. Imberger, and Y. Niño. 2008. The evolution of internal waves  
570       in a rotating, stratified, circular basin and the influence of weakly nonlinear and  
571       nonhydrostatic accelerations. *Limnol. Oceanogr.* **53**: 2738–2748.  
572       doi:10.4319/lo.2008.53.6.2738

573   de la Fuente, A., K. Shimizu, Y. Niño, and J. Imberger. 2010. Nonlinear and weakly  
574       nonhydrostatic inviscid evolution of internal gravitational basin-scale waves in a large,  
575       deep lake: Lake Constance. *J. Geophys. Res.* **115**: C12045. doi:10.1029/2009JC005839

576   Lazerte, B. D. 1980. The dominating higher order vertical modes of the internal seiche in a  
577       small lake. *Limnol. Oceanogr.* **25**: 846–854. doi:10.4319/lo.1980.25.5.0846

578   Lemckert, C., J. Antenucci, A. Saggio, and J. Imberger. 2004. Physical Properties of  
579       Turbulent Benthic Boundary Layers Generated by Internal Waves. *J. Hydraul. Eng.* **130**:  
580       58–69. doi:10.1061/(ASCE)0733-9429(2004)130:1(58)

581   Maas, L. R. M., and F.-P. A. Lam. 1995. Geometric focusing of internal waves. *J. Fluid*  
582       *Mech.* **300**: 1–41. doi:10.1017/S0022112095003582

583   Münnich, M., a. Wüest, and D. M. Imboden. 1992. Observations of the second vertical mode  
584       of the internal seiche in an alpine lake. *Limnol. Oceanogr.* **37**: 1705–1719.  
585       doi:10.4319/lo.1992.37.8.1705

586   Pernica, P., M. G. Wells, and W. G. Sprules. 2013. Internal waves and mixing in the  
587       epilimnion of a lake affects spatial patterns of zooplankton in a body-size dependent  
588       manner. *Limnol. Oceanogr. Fluids Environ.* **3**: 279–294. doi:10.1215/21573689-  
589       2409149

- 590 Phillips, O. 1977. *The Dynamics of the Upper Ocean*, 2nd ed. Cambridge Univ Press.
- 591 Posada-Bedoya, A., A. Gómez-Giraldo, and R. Román-Botero. 2022. Decoupled basin-scale  
592 internal waves in a continuously stratified two-basin tropical Andean reservoir.  
593 *Limnologica* **93**: 125931. doi:10.1016/j.limno.2021.125931
- 594 Posada-Bedoya, A., A. Gómez-Giraldo, and R. Román Botero. 2019. Preliminary  
595 characterization of the dominant baroclinic modes of a tropical Andean reservoir during  
596 a dry period. *Rev. la Acad. Colomb. Ciencias Exactas, Físicas y Nat.* **43**: 297.  
597 doi:10.18257/raccefy.799
- 598 Posada-Bedoya, A., A. Gómez-Giraldo, and R. Román-Botero. 2021. Effects of riverine  
599 inflows on the climatology of a tropical Andean reservoir. *Limnol. Oceanogr.*  
600 *lno.11897*. doi:10.1002/lno.11897
- 601 Román-Botero, R., A. Gómez-Giraldo, and M. T. Botero. 2013. Efecto estacional de los  
602 afluentes en la estructura térmica de un pequeño embalse neotropical, La Fe - Colombia.  
603 *Dyna* **80**: 152–161.
- 604 Serra, T., J. Vidal, X. Casamitjana, M. Soler, and J. Colomer. 2007. The role of surface  
605 vertical mixing in phytoplankton distribution in a stratified reservoir. *Limnol. Oceanogr.*  
606 **52**: 620–634. doi:10.4319/lo.2007.52.2.0620
- 607 Shimizu, K., and J. Imberger. 2008. Energetics and damping of basin-scale internal waves in  
608 a strongly stratified lake. *Limnol. Oceanogr.* **53**: 1574–1588.
- 609 Simpson, J. H., P. J. Wiles, and B. J. Lincoln. 2011. Internal seiche modes and bottom  
610 boundary-layer dissipation in a temperate lake from acoustic measurements. *Limnol.*  
611 *Oceanogr.* **56**: 1893–1906. doi:10.4319/lo.2011.56.5.1893

612 Sutherland, B. R. 2010. Internal Gravity Waves,.

613 Thorpe, S. a. 1998. Some dynamical effects of internal waves and the sloping sides of lakes.  
614 Phys. Process. Lakes Ocean. Coast. Estuar. Stud. **54**: 441–460.

615 Turner, J. S. 1973. Buoyancy Effects in Fluids, Cambridge University Press.

616 Ulloa, H. N., K. B. Winters, A. de la Fuente, and Y. Niño. 2015. Degeneration of internal  
617 Kelvin waves in a continuous two-layer stratification. J. Fluid Mech. **777**: 68–96.  
618 doi:10.1017/jfm.2015.311

619 UNESCO. 1981. Tenth report of the joint panel on oceanographic tables and standards. Tech.  
620 Pap. Mar. Sci. No. 36 24.

621 Vidal, J., and X. Casamitjana. 2008. Forced Resonant Oscillations as a Response to Periodic  
622 Winds in a Stratified Reservoir. J. Hydraul. Eng. **134**: 416–425.  
623 doi:10.1061/(ASCE)0733-9429(2008)134:4(416)

624 Vidal, J., S. MacIntyre, E. E. McPhee-Shaw, W. J. Shaw, and S. G. Monismith. 2013.  
625 Temporal and spatial variability of the internal wave field in a lake with complex  
626 morphometry. Limnol. Oceanogr. **58**: 1557–1580. doi:10.4319/lo.2013.58.5.1557

627 Wiegand, R. C., and V. Chamberlain. 1987. Internal waves of the second vertical mode in a  
628 stratified lake. Limnol. Oceanogr. **32**: 29–42. doi:10.4319/lo.1987.32.1.0029

629 Woodward, B. L., C. L. Marti, J. Imberger, M. R. Hipsey, and C. E. Oldham. 2017. Wind  
630 and buoyancy driven horizontal exchange in shallow embayments of a tropical  
631 reservoir: Lake Argyle, Western Australia. Limnol. Oceanogr. **62**: 1636–1657.  
632 doi:10.1002/lno.10522

633 Wüest, A., and A. Lorke. 2003. Small-Scale Hydrodynamics in Lakes. *Annu. Rev. Fluid*  
634 *Mech.* **35**: 373–412. doi:10.1146/annurev.fluid.35.101101.161220

635

1

2 VERTICALLY PROPAGATING SEICHES AND STANDING MODES PRECLUSION  
3 IN A STEEP-BOTTOM TROPICAL RESERVOIR

4

5 Andrés Posada-Bedoya<sup>1</sup>, Andrés Gómez-Giraldo<sup>2</sup>, Ricardo Román-Botero<sup>3</sup>

6

7 DRAFT

8 February 2024

9

10 Running head: Vertically propagating seiches

11

12 <sup>1,2,3</sup>Department of Geosciences and Environment, Universidad Nacional de Colombia, Calle  
13 59A No 63-20, Medellín, Colombia.

14 <sup>1</sup>Now at Department of Civil Engineering, Queen's University, Kingston, Ontario, ON K7L  
15 3N6, Canada

16 <sup>1</sup>Corresponding author. Email: 21afpb@queensu.ca

17 <sup>2</sup>Email: eagomezgi@unal.edu.co

18 <sup>3</sup>Email: rroman@unal.edu.co

19 Keywords: vertical propagation, standing waves, supercritical reflection, steep lake

20 **Abstract**

21 This work investigates observations of gradual upward phase shifting of temperature  
22 oscillations in a steep tropical reservoir, which differ from the  $\pi$  radians sharp shifts that are  
23 usually accepted for the description of baroclinic motions in terms of normal modes.  
24 Supported on numerical modeling and theoretical inviscid wave ray tracing, we show that  
25 the gradual upward phase shifting is the signature of vertically propagating seiches, which  
26 refer to basin-scale oscillations that are stationary in the horizontal but propagate downwards  
27 in the vertical. We show that the vertically propagating seiche occurs due to the predominant  
28 supercritical reflection of the internal wave rays at the lake boundaries, which focuses the  
29 internal wave energy downwards with a minor fraction of the energy reflected upwards,  
30 resulting in a net downward energy propagation. The net downward energy flux precludes  
31 the formation of standing waves, with potential implications for the common framework of  
32 the energy flux path at the interior of stratified lakes. The analysis supports that vertically  
33 propagating seiches and standing mode preclusion are expected to occur in any given lake,  
34 but their signatures are more evident in steep sided lakes, with a wide metalimnion and/or  
35 for lower forcing frequencies, characteristic of higher order vertical modes.

36

37 **Plain Language Summary**

38 In stratified lakes, large scale perturbations like those generated by the wind propagate as  
39 internal waves, with oscillatory motions of the particles that propagate in trajectories forming  
40 an angle with the horizontal. When they bounce at the lake contour, change direction but  
41 keep the angle of propagation respect to the horizontal plane. Incident and reflected waves

42 superpose and, under the ideal condition of no energy losses, form stationary basin scale  
43 internal waves, with points where there are no oscillations of the particles, which are called  
44 nodes. Although there is some energy loss along the propagation of the waves, in several  
45 cases they are small and natural mode theory describes the reality closely, so it is common  
46 to describe basin-scale periodic motions in terms of standing waves. We investigated  
47 observations of oscillatory basin-scale motions in a steep-sided tropical reservoir that are not  
48 stationary but have nodes that propagate upwards, which is a signature of wave energy  
49 propagating downwards. We show that this is the result of the reservoir sides being steeper  
50 than the trajectories of propagation of the waves, leading to accumulation of energy in the  
51 lake bottom instead of a reflection that allows for stationary waves to form.

52

### 53 **Key points**

- 54 • Net downward internal wave energy flux can occur in stratified lakes due to the  
55 imperfect reflection of internal wave rays.
- 56 • Predominant supercritical reflection of the internal wave rays at the lake boundaries  
57 results in a net downward energy propagation.
- 58 • Net downward energy propagation is more evident in steep lakes, lakes with a wide  
59 metalimnion and/or at lower forcing frequencies.

## 60 **1. Introduction**

61 The classical interpretation of coherent basin-scale internal motions in stratified lakes and  
62 reservoirs has been based on the decomposition onto its natural non-dissipative oscillation  
63 modes. This approach has been useful to understand the complex field of baroclinic motions  
64 at the basin scale and their energy flux path through the interactions of modes with the  
65 topography (Kocsis et al. 1998; Vidal et al. 2013), between modes (de la Fuente et al. 2008,  
66 2010), with the bottom boundary layer (Lemckert et al. 2004; Simpson et al. 2011) and with  
67 the turbulent field (Boegman et al. 2003; Gómez-Giraldo et al. 2008; Ulloa et al. 2015), which  
68 finally impact water quality through mixing and transport (Evans et al. 2008; Pernica et al.  
69 2013).

70 Strictly speaking, pure non-dissipative modes do not exist in real sloping bottom lakes  
71 (Shimizu and Imberger 2008) because the irregular bathymetry creates some residual  
72 unbalance between focusing and defocusing of some wave rays so they do not close upon  
73 themselves (Maas and Lam 1995; Thorpe 1998). Focusing of wave rays also concentrates  
74 energy and enhances viscous dissipation so the reflected rays have less energy than the  
75 incident rays, resulting in some degree of energy net downward propagation as upward and  
76 downward propagating rays do not have the same energy. In some cases, the energy net  
77 vertical flux is negligible, and the internal mode approach leads to good agreement with  
78 observations (Shimizu and Imberger 2008; Imam et al. 2013), while in other cases such  
79 approach is unable to approximate some characteristics of the oscillatory internal motions  
80 (Henderson and Deemer 2012). For instance, the internal mode approach predicts sharp  
81 changes of phase through the water column, while gradual changes of phase have been  
82 observed in several reservoirs (Lazerte 1980; Vidal and Casamitjana 2008; Henderson 2016).

83 Therefore, it is very pertinent to understand when the classical description of the oscillatory  
84 motions in terms of modes is inappropriate and should be precluded, and what else is  
85 necessary to better understand and describe the energy flux path at the interior of lakes  
86 (Imberger 1998; Wüest and Lorke 2003).

87 The bulk of research on baroclinic oscillations has focused on natural mild slope lakes, with  
88 predominant subcritical slopes, where most of the downward propagating energy introduced  
89 by the wind is reflected upwards at the bottom, allowing for standing waves formation. In  
90 those cases, the internal wave field can be well described in terms of the non-dissipative  
91 modes and perfect reflections can be considered. Conversely, in steep bottoms systems,  
92 slopes may be mostly supercritical and focus wave energy downwards upon reflection,  
93 reducing the upward wave energy available for the interference necessary to produce  
94 standing modes, so the resulting basin-scale oscillations after superposition are stationary in  
95 the horizontal but propagate downwards in the vertical, and standing waves do not develop,  
96 as first hypothesized by Thorpe (1998) and evidenced by Henderson and Deemer (2012).  
97 Following Henderson and Deemer (2012) and Henderson (2016), we call them vertically  
98 propagating seiches. In such a case, an upward phase shifting with depth of the temperature  
99 and velocity fluctuations is a clear signature of downward energy flux (Henderson and  
100 Deemer 2012). As steep lakes have been far less studied, the robustness of the non-dissipative  
101 mode model has not been thoroughly explored, so it is important to investigate conditions for  
102 its preclusion and identify the characteristics of the vertically propagating seiches when the  
103 mode is not formed.

104 This work is motivated by observations and numerical modeling in a steep reservoir that  
105 showed a coherent gradual vertical shifting in the phase of horizontal mode one basin-scale

106 oscillations with depth, very different from the  $\pi$  radians sharp shifts that are usually accepted  
107 for the description of baroclinic motions in terms of normal modes. Supported on numerical  
108 modeling and theoretical tracing of wave rays, we identify these motions as vertically  
109 propagating net oscillations, produced by the superposition of downward propagating waves  
110 and upward propagating reflected waves which are less energetic due to the dominant  
111 supercritical reflection of internal waves at the lake sloping bottom. We discuss the role of  
112 the sloping bottom on the standing mode preclusion and provide some context of our results  
113 respect to other lakes, supported on previously proposed parameterizations.

114

## 115 **2. Theoretical background**

116 Inviscid internal waves in a stratified fluid can be seen as a set of rays, whose energy  
117 propagates at an angle  $\theta$  respect to the horizontal, depending on the background stratification,  
118 characterized by the buoyancy frequency  $N$ , and wave frequency  $\omega$ :

$$\sin \theta = \frac{\omega}{N} \quad (1)$$

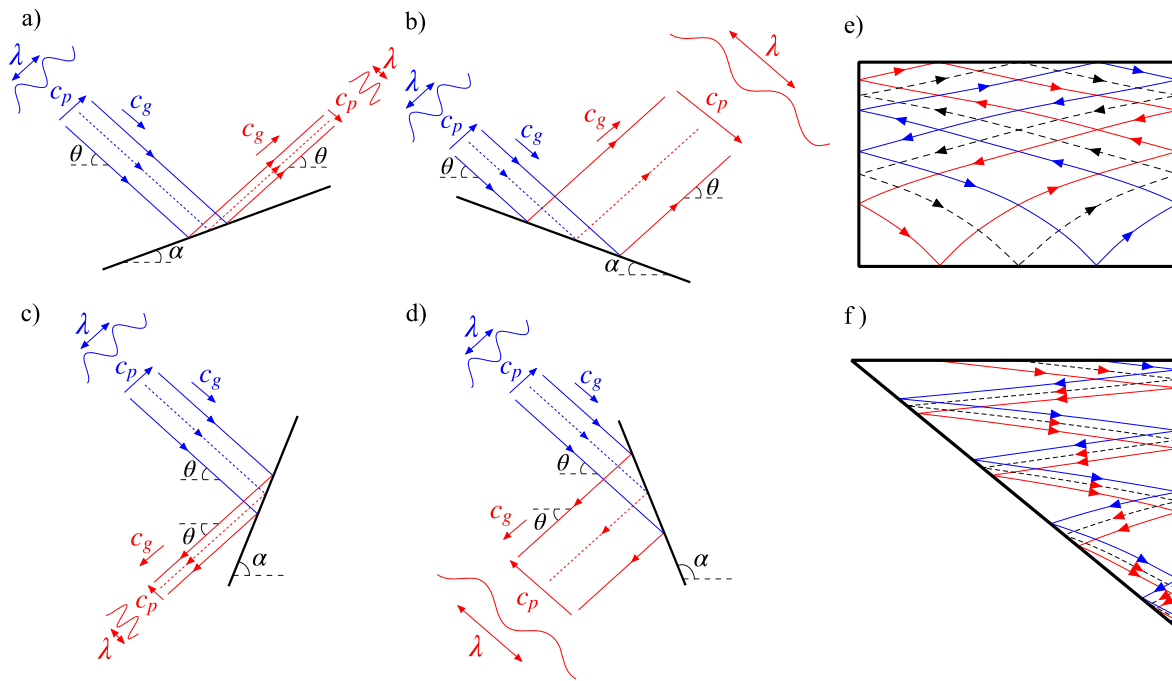
119 The fluid particle velocity  $\vec{u}$  is orthogonal to the phase velocity  $\vec{c}_p = \omega/\vec{k}$ , where  $\vec{k}$  is the  
120 wavenumber vector. The direction of energy propagation coincides with the direction of the  
121 particle motions, so the group velocity  $\vec{c}_g$  and  $\vec{c}_p$  are orthogonal with opposite vertical  
122 components (Turner 1973), such that downward (upward) wave energy flux is accompanied  
123 by upward (downward) phase propagation (Figure 1).

124 Internal wave rays maintain their propagating angle with the horizontal plane ( $\theta$ ) upon  
125 reflection at a solid boundary (Maas and Lam 1995), so incident and reflected rays make  
126 different angles to the sloping bottom, leading to wavelength change upon reflection (Fig. 1).

127 A decrease in wavelength after reflection is known as focusing (Fig. 1a, c) and a increase as  
128 defocusing (Fig. 1b, d). When the bottom slope  $\alpha$  is milder than that of the ray ( $\alpha < \theta$ ), the  
129 reflection is subcritical and the ray shifts its vertical direction of propagation upon reflection,  
130 so downward propagating waves are reflected upwards (Fig. 1a, b). If the boundary slope is  
131 steeper than the ray ( $\alpha > \theta$ ), downward propagating rays continue traveling downwards  
132 upon reflection (Fig. 1c, d). When wave energy propagation and bottom slopes are similar,  
133 i.e. close to the critical condition, large wave energy concentration (focusing) leads to a large  
134 amplitude reflected wave which turns into turbulence by overturning instability (Dauxois et  
135 al. 2004), with large wave energy loss, so the reflected wave is far less energetic than the  
136 incident one.

137 Standing waves occur when opposite identical progressive waves interfere. Because of the  
138 inclined paths of individual wave rays in stratified flows (eq. 1), the condition for standing  
139 modes to form is that every wave ray closes upon itself after bouncing from the boundaries  
140 (Fig. 1e) (Cushman-Roisin et al. 1989; Maas and Lam 1995). Moreover, because of the  
141 irregular bottom in natural basins, for a given forcing frequency there are always some rays  
142 that do not close upon themselves, so standing wave excitation is not perfect, and some  
143 degree of energy downward propagation always remains. Also, viscous dissipation and  
144 transference to turbulence reduces energy in the waves as they travel through the basin and  
145 bounce at the boundaries, so the upward reflected waves are less energetic, and upon  
146 interference with the downward waves, a residual downward propagation remains. These  
147 energy losses are small in mild slope natural lakes with significant subcritical reflection  
148 (Wiegand and Chamberlain 1987; Münnich et al. 1992; Imam et al. 2013). In some cases,  
149 most of the wave rays can be trapped by successive reflections at the boundaries towards

150 particular regions of the basin, like the shore or the bottom, and no longer close upon  
 151 themselves, precluding standing waves (Thorpe 1998). In particular, when supercritical  
 152 reflection is dominant, wave rays are focused towards the bottom and a minor fraction of  
 153 energy is reflected upwards to conform the standing wave such that downward propagating  
 154 waves dominate because of the difference in downward and upward energy fluxes (Fig. 1f)  
 155 (Henderson and Deemer 2012).



156  
 157 **Figure 1.** Schematic of wave rays reflecting at a (a, b) subcritical and (c, d) supercritical solid  
 158 boundary (a, c) focusing and (b, d) defocusing. Blue and red lines denote the lines of constant  
 159 phase of incident and reflected waves respectively and arrows indicate the direction of energy  
 160 propagation. Dashed and continuous lines indicate trough and peaks of the wave respectively.  
 161 Schematic of wave ray paths for (e) a standing mode (every wave ray closes upon itself) and  
 162 (f) vertically propagating seiche in a supercritical basin (wave rays are trapped at the bottom).  
 163

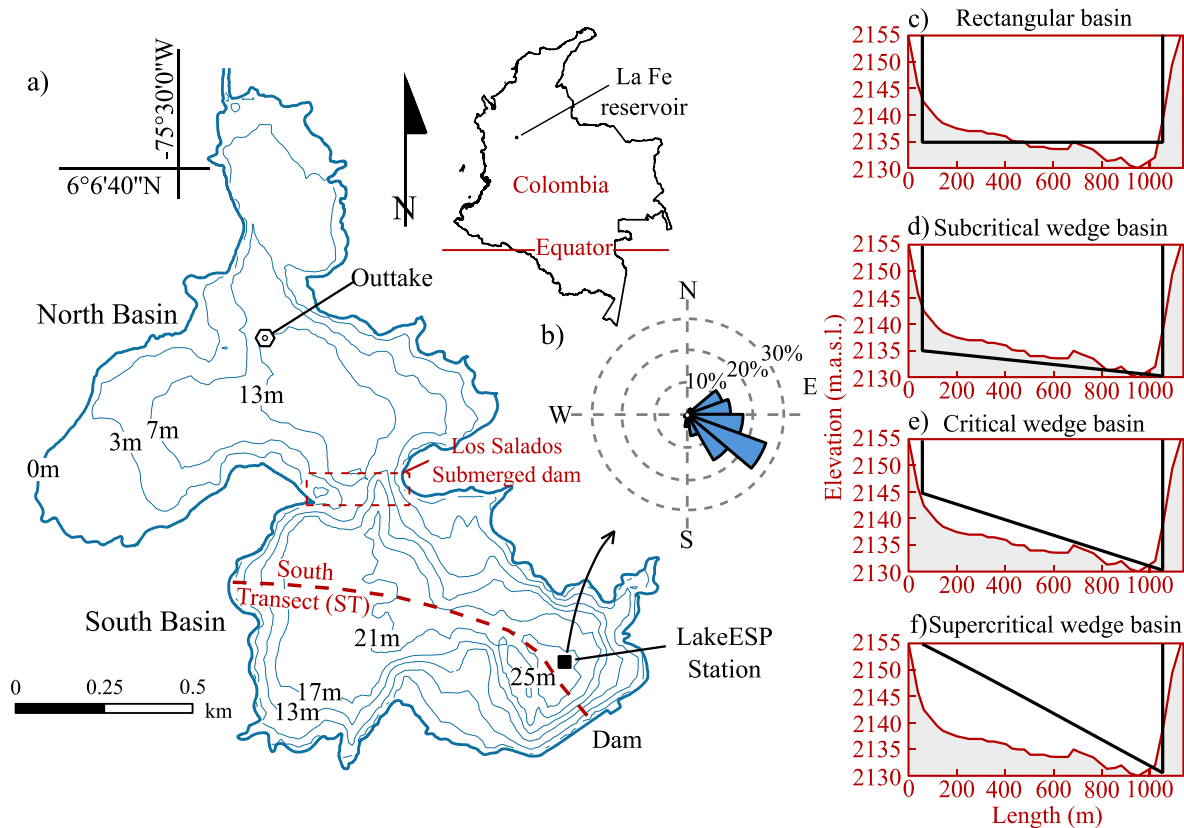
164 **3. Materials and methods**

165 3.1. Study site and field measurements

166 La Fe is a tropical reservoir located in the Northwest of Colombia (06°06'40"N,  
167 75°30'00"W) at 2150 m.a.s.l. on the Andean Mountain range (Fig. 2). This tropical Andean  
168 reservoir remains thermally stratified through the year, with seasonal changes ruled by the  
169 inflow discharge (Román-Botero et al. 2013; Posada-Bedoya et al. 2021; Posada-Bedoya et  
170 al. 2022). The reservoir is composed of two basins (North and South) separated by a shallow  
171 and narrow neck formed by the old-submerged dam Los Salados.

172 After Posada-Bedoya et al. (2022) showed that internal oscillations in each basin are  
173 decoupled, we will focus here on the South basin, where a LakeESP platform equipped with  
174 a thermistor chain and a meteorological station was installed close to the dam site (Fig. 2) to  
175 collect data every 5 min from 6 to 22 September 2012. Thirteen temperature loggers were  
176 hanging from the float at depths of 0.7, 1.5, 2.3, 3.0, 3.8, 4.5, 5.3, 6.1, 7.3, 9.1, 11.2, 13.2,  
177 15.2 m, and one additional thermistor was moored 1 m above the lake bottom. Temperature  
178 loggers had a resolution of 0.0001°C and an accuracy of 0.01°C. The meteorological station  
179 measured air temperature, atmospheric pressure, relative humidity, net shortwave and  
180 longwave radiation, rainfall, and wind speed and direction.

181 The periodic wind excites 24, 12 and 6-h basin-scale horizontal mode 1 oscillations in the  
182 South basin that are decoupled and have different vertical structure in both basins of the  
183 reservoir (Posada-Bedoya et al. 2022). The more energetic mode shows a vertical structure  
184 that resembles that of a stationary vertical mode 4, so it could be classified as a V4H1 mode.  
185 However, sharp phase changes between layers, as are predicted by normal modes, were not  
186 observed and a coherent gradual shift with depth in the phase was observed instead.



187

188 **Figure 2.** (a) Location and bathymetry of La Fe reservoir and LakeESP station location. (b)  
 189 Wind rose for wind speeds faster than  $2.5 \text{ m s}^{-1}$ . (c-f) Bottom elevation along the South  
 190 transect shown in (a) (red line) and wedge basins for numerical experiments (black line).

191

### 192 3.2. Hydrodynamic modeling

193 Numerical experiments with the 3D hydrodynamic model AEM3D were conducted to  
 194 understand the nature of the diurnal oscillations in La Fe South basin, and to explore the  
 195 effect of the sloping bottom.

196

197 *3.2.1. AEM3D model*

198 The Aquatic Ecosystem Model (AEM3D) (Hodges and Dallimore 2016) solves the three-  
199 dimensional (3D), hydrostatic, Boussinesq, Reynolds-averaged Navier-Stokes equations, and  
200 scalar transport equations in a z-coordinate system, using a finite-difference discretization of  
201 momentum and a finite-volume discretization of conservation of mass (Hodges 2000;  
202 Hodges and Dallimore 2016). The free surface evolution is modeled implicitly, while  
203 advection of momentum and scalars are solved explicitly with an Euler-Lagrangian scheme  
204 and an ULTIMATE-QUICKEST scheme, respectively (Hodges 2000; Hodges and Dallimore  
205 2016). The model uses UNESCO (1981) equation of state to relate temperature and density.  
206 The mixed-layer algorithm computes vertical mixing throughout the water column based on  
207 an integral model of the turbulent kinetic energy equation (Hodges 2000). Horizontal mixing  
208 is solved through an eddy viscosity model. No-slip and zero normal flow boundary conditions  
209 are imposed at bottom and lateral boundary cells. Because of the staircase representation of  
210 the bottom, the model slightly overestimates numerical diffusion and internal wave damping  
211 (Gómez-Giraldo et al. 2006; Vidal et al. 2013), despite which it has been demonstrated to  
212 accurately predict basin-scale internal waves in a wide variety of lakes and reservoirs  
213 worldwide (Vidal et al. 2013; Woodward et al. 2017; Dissanayake et al. 2019).

214

215 *3.2.2. Numerical experiments*

216 After calibration of the AEM3D model with temperature records from a thermistor chain  
217 (Posada-Bedoya et al. 2021), we conducted five two-dimensional numerical experiments:  
218 one for a basin with the bottom profile of the decoupled South basin (South Transect in Fig.  
219 1) and the other four for idealized vertical walls wedge-shaped basins with different bottom

220 slopes (Fig. 2c-f). To simulate 2D basin geometries with the 3D model, we setup the  
221 bathymetry of each scenario in the  $x$ - $z$  plane (Fig. 2c-f), with an individual cell in the  
222 spanwise direction and a free-slip boundary condition on the sidewalls. Results were  
223 insensitive to the spanwise cell size.

224 For each scenario, the domain was discretized using a uniform horizontal grid of 25 m and  
225 0.4 m uniform thick layers (Table 1). We verified grid independency of the results at this  
226 spatial resolution. The time step was 10 s to meet the numerical stability condition for the  
227 internal motions. We simulated the response in each case to the forcing of an idealized wind  
228 with a speed  $v = v_0 \cos(\omega t)$ , with  $v_0 = 3 \text{ m s}^{-1}$  and a frequency  $\omega = 7.27 \times 10^{-5} \text{ s}^{-1}$  (24 h  
229 period) in the case with the shape of the South basin, as it was the period of the dominant  
230 oscillations observed in the field (Posada-Bedoya et al. 2022). For the idealized wedge  
231 basins, the forcing period was 20 h, which is the period of the theoretical V4H1 mode of the  
232 rectangular basin, according to Gill (1982) eigenmodel for the average stratification of the  
233 survey (Fig. 3b). We ran the model without other external forcing, i.e. with no other  
234 meteorological inputs than the wind, inflows, or outflows. By simulating the basins with a  
235 perfectly periodic wind forcing, we are considering the most favorable condition for the  
236 standing mode excitation in each case. The model ran for 9 days, enough time for the  
237 excitation of a standing wave, before mixing modifies the background stratification and the  
238 natural modes characteristics. The model was initialized with the average stratification of the  
239 survey (Fig. 3b), with horizontally homogeneous layers and zero velocity everywhere. The  
240 simulations were carried out using default model parameters, which were based on non-site-  
241 specific literature values (Hodges and Dallimore 2013), as in other modelling studies  
242 (Woodward et al. 2017).

243 Based on the forcing period of the idealized wedge scenarios and the minimum value of the  
 244 buoyancy frequency ( $N_{min}=0.0057$  Hz) (Fig. 3b), the critical slope ( $\theta_c = 2\pi\omega/N_{min}$ ) was  
 245 0.0153 rad, on which we relied to define the bottom slope of the wedges ( $\alpha$ ) as subcritical  
 246 ( $\alpha < 0.7\theta_c$ ), critical ( $0.7\theta_c < \alpha < 1.5\theta_c$ ) and supercritical ( $\alpha > 1.5\theta_c$ ), similar to what was  
 247 used in previous studies (Gómez-Giraldo et al. 2006; Henderson and Deemer 2012) (Table  
 248 1).

249 **Table 1.** Parameters for the setup of numerical experiments.

Scenario	$\alpha$ (rad)	$\alpha/\theta_c$	Maximum depth $H$ (m)	Length $L$ at $H/2$ depth (m)
Rectangular	0.000	0.00	20	1000
Subcritical	0.005	0.33	25	1000
Critical	0.015	0.98	25	850
Supercritical	0.025	1.63	25	500
South basin	----	----	27	1100

250

### 251 3.2.3. Analysis of model results

252 The vertical structure of the oscillations was identified from calculations of wavelet  
 253 coherence and phase (Grinsted et al. 2004) for series of temperature profiles close to the  
 254 deepest edge of the basin, and by band-pass filtering the time series of horizontal velocity  
 255 profiles predicted by the 3-D model using a fourth-order Butterworth filter.

256

### 257 3.3. Wave ray tracing

258 For each scenario, we traced the path in the time-depth ( $t-z$ ) space of constant phase lines of  
 259 linear shallow water progressive WKB waves (Phillips 1977). At a fixed horizontal position,  
 260 wave crests move vertically at speed  $c_z = \omega/k_z$  (Sutherland 2010), so constant phase lines  
 261 paths are given by

$$\frac{dz}{dt} = c_z = \frac{2\pi\omega^2\lambda_x}{N(z)} \quad (5)$$

262 where  $\lambda_x$  is the horizontal wavelength and  $k_z$  is the vertical component of the wavenumber  
 263 vector. We traced constant phase lines every  $T/2$  by solving eq. 5 at discrete time steps,  
 264 starting at the bottom in the center of the basin. We compared the path of constant phase lines  
 265 to the time-depth structure of the band-passed simulated horizontal velocity, accepting that a  
 266 close agreement indicates vertical propagation Henderson and Deemer (2012). In all the  
 267 wedge cases, the stratification and forcing frequency were the same, thus the differences in  
 268 the paths were only due to the selected wavelength  $\lambda_x$ , in this case  $2L$ , as the basin-scale  
 269 waves observed in the lake are horizontal-one (Posada-Bedoya et al. 2022), and  $L$  being the  
 270 length of the basin at the middle depth (Table 1). The path of wave ray energy in the length-  
 271 depth ( $x$ - $z$ ) space of each basin for the given forcing frequency was calculated from:

$$\frac{dz}{dx} = \tan \theta \quad (6)$$

272 Differences in wave energy paths in the wedge basins were only due to the basin geometry,  
 273 which determines the distance traveled by wave rays at different depths as they repeatedly  
 274 cross the lake and reflect from end walls while propagating from surface to bed (or from bed  
 275 to surface). Energy wave packet was not traced in the south basin because the wave ray  
 276 propagation occurs in a three-dimensional space.

277

### 278 3.4. Reflection coefficient

279 The reflection coefficient is the fraction of incident wave energy that is reflected at the lake  
 280 bottom (Henderson and Deemer 2012; Henderson 2016). The closer it is to one, the closer

281 the superposition of down and upward propagating waves is to a standing wave or natural  
 282 mode. In this work, it was calculated for each numerical experiment by adjusting the  
 283 theoretical interference pattern between downward (incident) and upward (reflected)  
 284 progressive waves to that of the modeling results. We estimated vertical profiles of power  
 285 and phase  $\hat{\psi}_M(z, \omega_0)$  of the internal wave forced at frequency  $\omega_0$  in AEM3D by computing  
 286 the Fourier transform  $\hat{\psi}_M(z, \omega)$  of the horizontal velocity signal  $u_M(z, t)$ , simulated at  
 287 several heights ( $z$ ) in the center of the basin:

$$u_M(z, t) = \sum_{\omega} \hat{\psi}_M(z, \omega) e^{i2\pi\omega t} \quad (2)$$

288 The theoretical profile of power and phase  $\hat{\psi}_T(z, \omega_0)$  for the wave forced at the frequency  
 289  $\omega_0$  was estimated as in Henderson (2016):

$$\hat{\psi}_T(z, \omega_0) = \left( \frac{N(z)}{N_0} \right)^{1/2} \hat{\psi}_{z_0} [e^{-i\phi_T(z, \omega_0)} + R e^{i\phi_T(z, \omega_0)}] \quad (3)$$

290 where  $R$  is the reflection coefficient,  $\hat{\psi}_{z_0}$  is the complex amplitude of downward-propagating  
 291 waves at the height of reference  $z_0$ ,  $N_0 = N(z_0)$ , and the theoretical phase between  $\hat{\psi}_{z_0}$  (at  
 292  $z_0$ ) and  $\hat{\psi}_T(z, \omega_0)$  at elevation  $z$  is:

$$\phi_T(z, \omega_0) = \int_{z'=z_0}^z \frac{2\pi}{\lambda_z} dz' = \int_{z'=z_0}^z \frac{N(z')}{\omega_0 \lambda_x} dz' \quad (4)$$

293 where  $\lambda_x$  and  $\lambda_z$  are the horizontal and vertical projections of the wavelength respectively.  
 294 We adjusted simultaneously  $R$ ,  $\lambda_x$  and  $\hat{\psi}_{z_0}$  by minimizing the squared error between  
 295  $\hat{\psi}_T(z, \omega_0)$  and  $\hat{\psi}_M(z, \omega_0)$  profiles, for  $\omega_0$  associated to the forcing period in each case. We  
 296 used AEM3D results above 15 m deep in the center of the basin, as below that depth the wave  
 297 rays are nearly vertical because of the reduced stratification (Fig. 3b), so the vertical

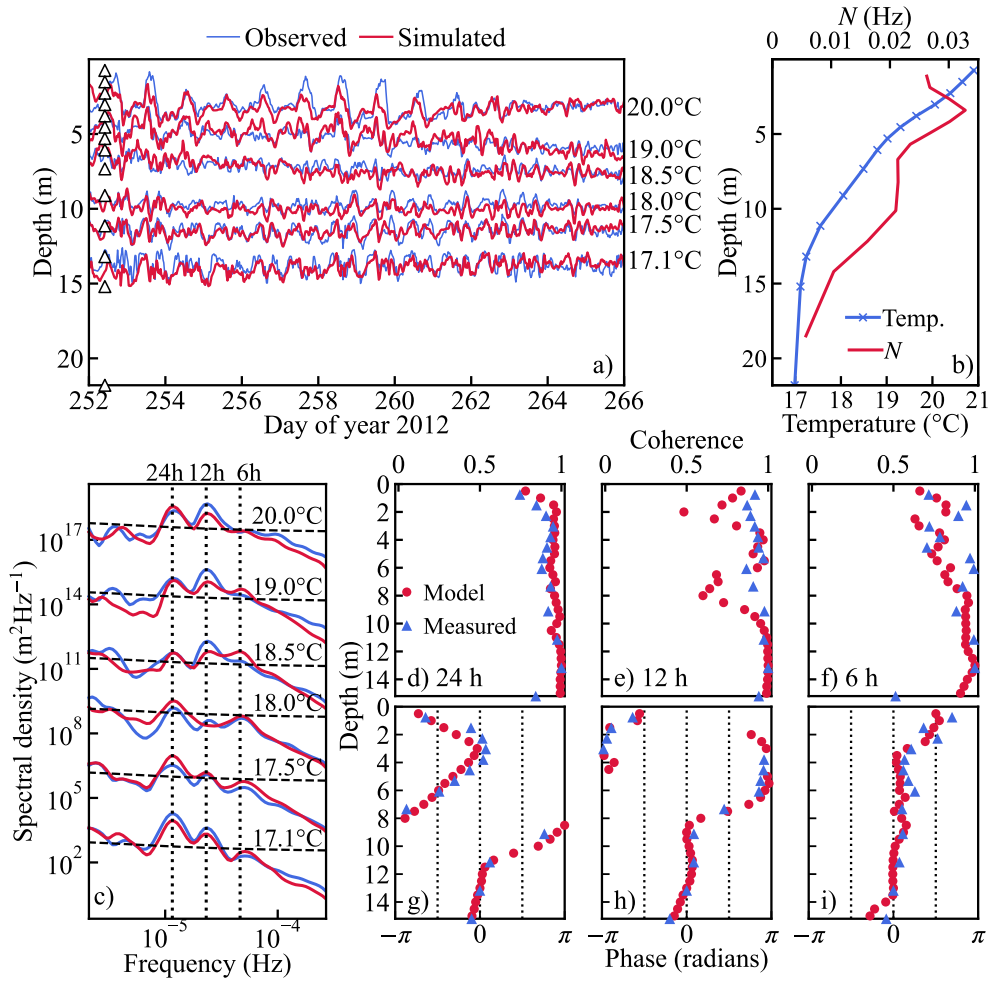
298 wavelength grows exponentially (eq. 4) and the energy profile is roughly uniform, similarly  
299 to Henderson (2016).

300

## 301 **4. Results**

### 302 4.1. Overview of field and model results

303 The background temperature vertical structure did not change significantly throughout the  
304 survey (Fig. 3a) and had a relevant gradient from the near surface down to ~14 m deep, and  
305 was nearly uniform below that depth (Fig. 3b). The wind speed exhibited a strong diel  
306 variability with the strongest winds coming from the East-Southeast (Fig. 1b) early in every  
307 afternoon and forcing internal waves with dominant periods of 24, 12 and 6 h in the South  
308 basin (Fig. 3c) oscillating along the east-west transect and being decoupled from those in the  
309 North basin (Posada-Bedoya et al. 2022). The 24-h oscillations exhibited a continuous phase  
310 shifting with depth in the top 15 m, gradually reversing direction (changing phase by  $\pi/2$   
311 radians) three times in both field and model results (Fig. 3d, g), which is indicative of vertical  
312 propagation of wave energy. The internal waves of 12-h and 6-h period exhibited structures  
313 resembling V2 (Fig. 3e, h) and V1 (Fig. 3f, i) oscillations.



314

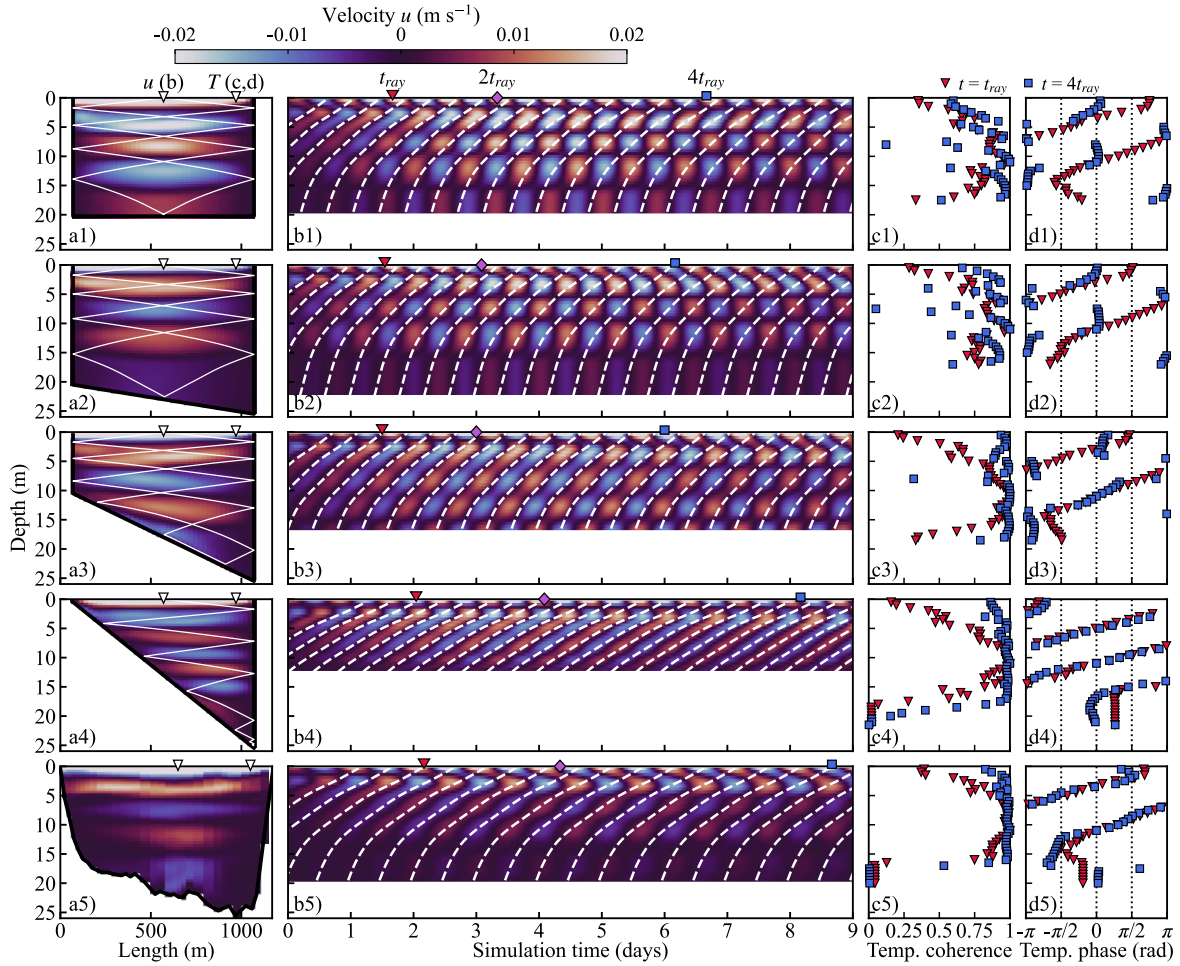
315 **Figure 3.** (a) Isotherm depths estimated from measurements and model results. The triangles  
 316 indicate the depth of the thermistors. (b) Average temperature and buoyancy frequency  
 317 profiles. (c) Global wavelet spectra of the observed (blue lines) and modeled (red lines)  
 318 isotherm displacements. Dashed line indicates the threshold for significant energy with a  
 319 95% confidence. Offset between spectra is three logarithmic cycles. Profiles of wavelet (d,  
 320 e, f) coherence and (g, h, i) phase of the temperature fluctuations of (d, g) 24 h, (e, h) 12 h  
 321 and (f, i) 6 h period oscillations. Coherence and phase are relative to the 13 m deep  
 322 temperature signal.

323

## 324 4.2. Periodically wind-forced basins

325 We define  $2t_{ray}$  as the time required for wave energy to travel downwards from the surface,  
326 bounce at the bottom and return to the surface. In all the scenarios, before a time  $\sim 2t_{ray}$ ,  
327 the phase profile of temperature oscillations exhibited a continuous upward shifting (Fig. 4d),  
328 indicating that before a time  $\sim 2t_{ray}$  the wave energy fluxed downwards as in a progressive  
329 wave, excited by the first cycle of wind forcing. Unlike vertically standing modes, the band-  
330 passed horizontal velocity in the time-depth space showed upward phase propagation  
331 matching the theoretical upward propagation of constant phase lines (Fig. 4b).

332 In the rectangular and subcritical basins, from a time  $\sim 2t_{ray}$  onwards the horizontal velocity  
333 in the time-depth space exhibited the arrangement of oscillating cells, characteristic of a  
334 standing mode (Fig. 4b1, b2 and Supplementary Videos 1 and 2). The coherence of  
335 temperature oscillations decreased at depths where phase shifts close to  $\pi$  radians occurred,  
336 suggesting the presence of nodes of vertical displacements in a standing wave (Fig. 4 c1, c2,  
337 d1, d2). The ray tracing predicted wave rays closing upon themselves for wave periods of  
338 19.4 and 18.9 h for rectangular and subcritical cases respectively (Fig. 4a1, a2), after  
339 bouncing four times at each lateral wall, in agreement with the estimated V4H1 mode of 20-  
340 h period of the rectangular basin.



341

342 **Figure 4.** (a) Depth-length curtain of band-passed horizontal velocity at a time of maximum  
 343 kinetic energy. Panels 1-5 are respectively for rectangular, subcritical, critical, supercritical  
 344 and South basins. The white line in panels a1-a4 is the path of an energy wavepacket excited  
 345 at the center of the lake surface. (b) Time-depth contours of the band-passed horizontal  
 346 velocity in the center of the basin. White dashed lines show the path of theoretical constant  
 347 phase lines. Profiles of (c) coherence and (d) phase of temperature oscillations at the deepest  
 348 part of the basins (location indicated in panels a), at the times indicated by markers in panels  
 349 (b). Coherence and phase are relative to the 10 m deep temperature signal.

350

351 In the supercritical case the horizontal velocity structure in the time-depth space showed  
352 upward phase propagation consistent with the theoretical constant phase lines of progressive  
353 waves for the entire simulation (Fig. 4b4 and Supplementary Video 4). The coherence of  
354 temperature oscillations was high throughout the water column (Fig. 4c4), so nodes and  
355 antinodes characteristic of a standing wave did not occur, contrasting with the nodes and  
356 antinodes observed in the rectangular and subcritical cases. The continuous upward phase  
357 shifting remained throughout the simulation very similar to that before  $2t_{ray}$  (Fig. 4d4),  
358 suggesting a permanent downward propagation of energy and that standing modes of 20-h  
359 period were not formed, despite the ideal periodic forcing conditions for their excitation. The  
360 ray tracing in the  $x$ - $z$  space showed the continuous downward reflection at the boundaries  
361 and the consequent trapping of the wave energy at the bottom of the basin for waves of 20 h  
362 period (Fig. 4a4). The oscillations had a vertical structure higher than V4, due to the increase  
363 in the number of times the ray crosses the lake from side to side (Fig. 4a4), as the vertical  
364 wavelength ( $\lambda_z = 4\pi\omega L/N$ ) is shorter because of the smaller  $L$ .

365 The nearly critical case was a transitional condition between subcritical and supercritical  
366 cases. The phase showed a hybrid structure with  $\sim \pi$  radians shifts at some depths and  
367 upward shifting between 7 and 14 m (Fig. 4d3 and Supplementary Video 3). The coherence  
368 reductions were less marked than in the rectangular and subcritical cases (Fig. 4c3), even  
369 after several cycles of wind forcing, so nodes were not clearly developed. The wave ray  
370 closed upon itself for a period of 20.2 h, but propagated nearly parallel to the sloping bottom  
371 after reflection (Fig. 4a3), so the inviscid ray tracing is expected to be invalid because of the  
372 large dissipation associated to the instabilities associated to the nearly critical reflection  
373 expected in this region (Dauxois et al. 2004).

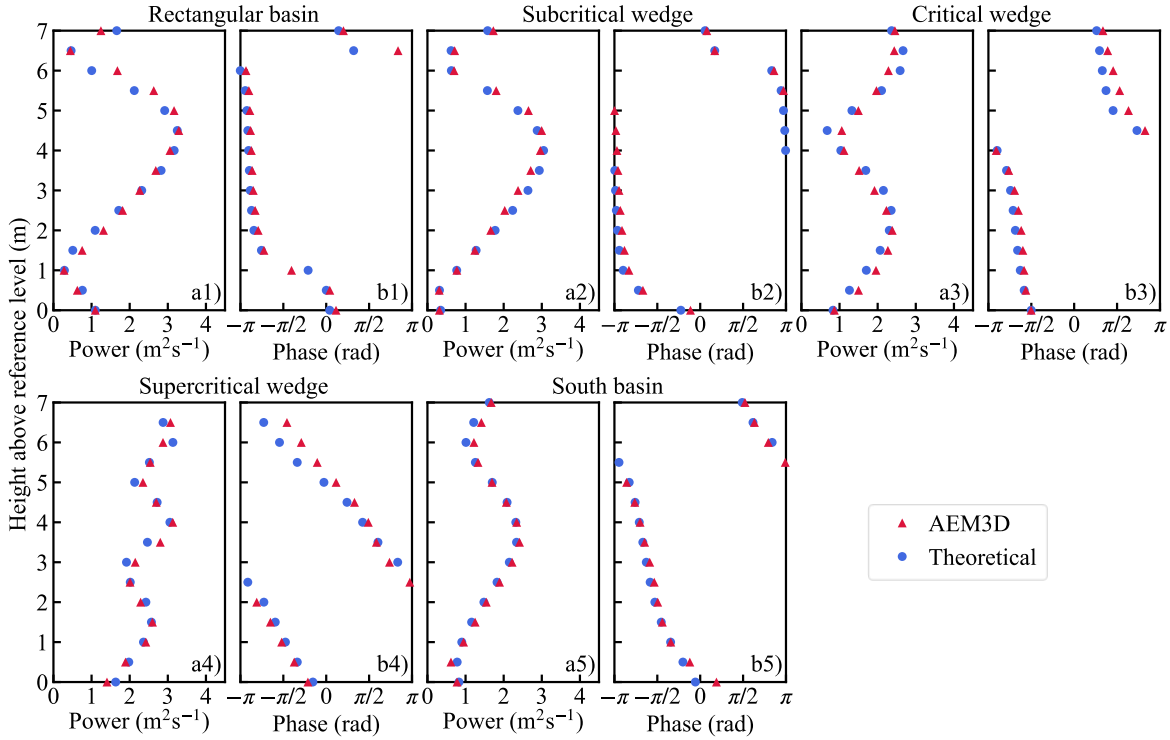
374 In the south basin experiment, as in the supercritical case, the horizontal velocity structure in  
375 the time-depth space did not develop the cell structure associated to standing modes, and  
376 instead, it kept the progressive wave signature, fitting the theoretical phase of progressive  
377 waves throughout the simulation (Fig. 4b5 and Supplementary Video 5). The phase structure  
378 of temperature oscillations maintained a gradual upward shifting (Fig. 4d5) like the one  
379 obtained from field measurements and the 3D simulation (Fig. 3g). Coherence was high  
380 throughout the water column, indicating nodes and antinodes did not occur (Fig. 4c5).  
381 According to this, despite the ideal periodic wind forcing, the standing mode of 24 h period  
382 was not formed and instead a vertically propagating internal seiche was excited. A very  
383 similar result was obtained when the system was forced with a 20-h period wind (not shown).  
384 As in the field and model validation, the phase profile reverses its slope around the depth of  
385 maximum  $N$  ( $\sim 3$  m), in agreement with the relation between phase and buoyancy frequency  
386 in eq. 4.

387

#### 388 4.3. Reflection coefficient

389 The theoretical pattern of interfering progressive waves fits very well to the power and phase  
390 profiles estimated from AEM3D results (Fig. 5), so the adjusted  $R$  and  $\lambda_x$  (Table 2) are  
391 reliable. The reflection coefficient is higher for the rectangular and subcritical cases and  
392 reduces dramatically for the supercritical scenario, while the nearly critical case poses a  
393 transition between both conditions. In the real bathymetry of the south basin, the reflection  
394 coefficient was between those for the critical and supercritical cases, in accordance with the  
395 signatures of vertical propagation shown above. The adjusted  $\lambda_x$  was always very close to  
396  $2L$  (cf.  $L$  at  $H/2$  depth in Table 1 to  $\lambda_x$  in Table 2), consistent with the horizontal-one

397 oscillations. Nodes and antinodes of a standing wave can be identified in the rectangular and  
 398 subcritical cases but are less evident as the bottom slope increases and in the south basin.



399

400 **Figure 5.** Power and phase profiles estimated from AEM3D results and from theoretical  
 401 interference between opposite progressive waves.

402 **Table 2.** Fitted reflection coefficient  $R$  and horizontal wavelength  $\lambda_x$  for each scenario.

Scenario	$\alpha/\theta_c$	$R$	$\lambda_x$ (m)
Rectangular	0.00	0.89	2000
Subcritical	0.33	0.85	2187
Critical	0.98	0.62	1711
Supercritical	1.60	0.14	1037
South basin	----	0.42	2378

403

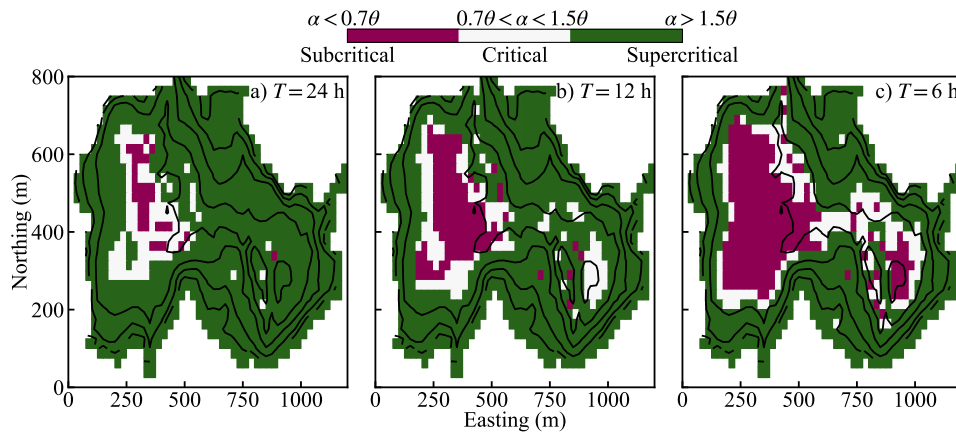
## 404 5. Discussion

### 405 5.1. Role of the sloping bottom on the vertical propagation

406 Numerical experiments indicate that diurnal standing waves were precluded in La Fe South  
407 basin and, instead, a 24-h period vertically propagating horizontal mode one seiche was  
408 observed. Comparing the slopes of the wave ray path (calculated with eq. 1 for the measured  
409 average buoyancy frequency at the bottom) and the bottom, we classified the reflection as  
410 subcritical ( $\alpha < 0.7\theta_c$ ), critical ( $0.7\theta_c < \alpha < 1.5\theta_c$ ) or supercritical ( $\alpha > 1.5\theta_c$ ) (Fig. 6a),  
411 and found that most of the reflections of 24-h period waves in the south basin are  
412 supercritical, explaining why a downward vertically propagating seiche is observed instead  
413 of a standing vertical mode. Because of the predominant supercritical reflection, internal  
414 wave energy is focused and trapped at the bottom, where it is expected to be the main source  
415 of energy for the bottom boundary layer, as in Henderson (2016), differing from the common  
416 framework of the energy flux path at the interior of stratified lakes (Imberger 1998; Wüest  
417 and Lorke 2003), with potential implications for mixing and transport processes that impact  
418 water quality.

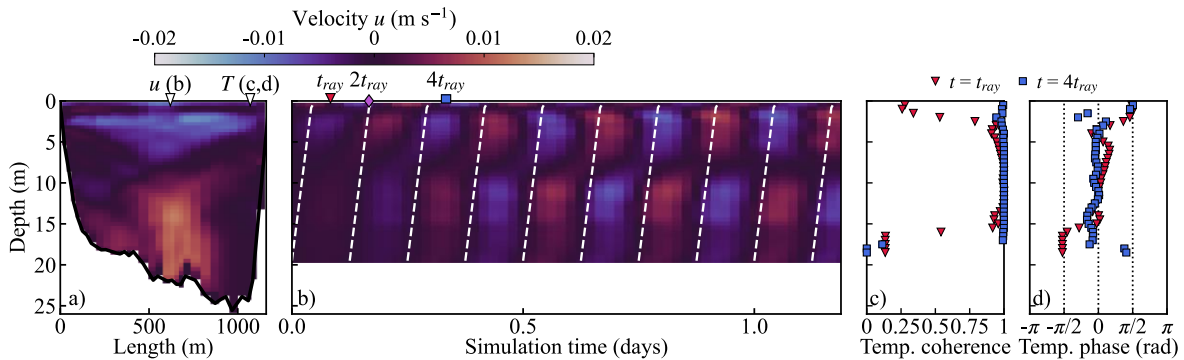
419 As the forcing frequency increases, the area where reflection is subcritical grows (Fig. 6) and  
420 more energy can be reflected upwards at the sloping bottom and standing waves can be  
421 observed. This is illustrated by forcing the south basin with 6-h period winds, which excite a  
422 coherent V1H1 response (Fig. 7) (Supplementary Video 6). Increasing supercritical  
423 reflection for lower forcing frequencies implies that higher order vertical motions are more  
424 likely to occur as vertically propagating seiches and are less suitable to be described as  
425 standing modes. This is consistent with the gradual phase shifting in the temperature and

426 velocity profiles, observed more often in lakes with dominant oscillations of high vertical  
 427 order (Lazerte 1980; Serra et al. 2007; Henderson and Deemer 2012).



428

429 **Figure 6.** Spatial classification of the sloping bottom of the South basin for wave periods of  
 430 (a) 24, (b) 12 and (c) 6 h.



431

432 **Figure 7.** Response of the South basin to a 6-h period forcing: (a) Curtain along the south  
 433 transect (ST) of band-passed horizontal velocity after one day of simulation, (b) Time-depth  
 434 contours of the band-passed horizontal velocity in the middle of the basin, with white dashed  
 435 lines showing the path of theoretical constant phase lines. (c) Coherence and (d) phase of  
 436 temperature profiles at the deepest edge of the basin (panels a) at the times indicated by  
 437 markers in panels (b).

438

439 5.2. Ubiquity of vertically propagating seiches

440 The reflection coefficient for the rectangular and subcritical cases was slightly lower than 1,  
441 indicating that the reflected energy was lower than the incident and a net residual downward  
442 energy propagation occurred, despite clear signatures of standing waves being identified in  
443 those cases. This shows that some degree of vertical propagation of basin-scale internal  
444 waves should always be expected, even in the simplest rectangular basin. Still, a large bulk  
445 of research has been conducted using the inviscid natural mode concept to describe basin-  
446 scale internal waves in lakes (Wiegand and Chamberlain 1987; Münnich et al. 1992; Imam  
447 et al. 2013).

448 We conjecture that vertically propagating seiches have not been widely explored because  
449 systems with adequate conditions for them to be clearly evident, like steep walls and wide  
450 metalimnion, have been far less studied. Most descriptions of basin-scale internal waves have  
451 been conducted in natural mild slope lakes, where a significant subcritical reflection occurs  
452 such that appreciable standing waves develop even if some small degree of vertical  
453 propagation remains, and in temperate systems with a thin metalimnion. In the latter case,  
454 the stratification is weak above (in the surface layer) and below (the hypolimnion) of the thin  
455 metalimnion, so wave ray paths are nearly vertical in those regions of the water column, and  
456 the phase shifting is mainly confined to within the thin metalimnion, making it difficult to  
457 distinguish the gradual phase shifting when occurring. Instead, in systems with a wide  
458 metalimnion, the signature of the gradual phase shifting with depth extends through a larger  
459 depth range, so it is more evident when occurring, as in some shallow summer temperate  
460 lakes (Lazerte 1980), temperate reservoirs with selective withdrawal at intermediate depths

461 (Serra et al. 2007), or tropical Andean reservoirs during moderate dry conditions (Posada-  
 462 Bedoya et al. 2019).

463 To provide a global context of the degree of vertical propagation in La Fe, in comparison  
 464 with other lakes, we estimated the parameters  $D = NH/(\pi\omega L)$  (Henderson and Deemer  
 465 2012) and reflection coefficient  $\mathcal{R}$  (Henderson 2016), defined in terms of readily available  
 466 variables measured in the field, for several systems where high order vertical modes were  
 467 dominant (Table 3). The parameter  $D$  is the ratio of mean lake ( $2H/L$ ) to wave ray ( $2\pi\omega/N$ )  
 468 slopes. High values of  $D$  are typical of steep and/or strongly stratified lakes, with dominant  
 469 supercritical reflection and vertical propagation, and low values are typical of mild slope  
 470 and/or weakly stratified lakes, with a dominant subcritical reflection that favors standing  
 471 waves excitation. The parameter  $\mathcal{R}$  is a parameterization of the reflection coefficient  $R$  in  
 472 terms of readily available variables measured in the field. It was estimated as (Henderson  
 473 2016):

$$\mathcal{R} = \frac{1 - \beta}{1 + \beta} \quad (8)$$

$$\beta = 2 \left( \frac{8}{\pi} \right)^{1/2} C_D \frac{v_{RMS}}{c_{gz}} \quad (9)$$

474 where  $C_D$  is the bottom drag coefficient,  $v_{RMS}$  is the root-mean-square of the velocity of the  
 475 internal waves induced currents, and  $c_{gz}$  is the vertical component of the group velocity,  
 476 with the same magnitude of the vertical phase velocity in eq. (5). A value of  $\mathcal{R} = 1$  indicates  
 477 perfect reflection. For the calculations, we assumed a typical value of  $C_D = 2 \times 10^{-3}$ , as in  
 478 Henderson (2016).

479 For all the selected cases,  $\mathcal{R} < 1$  and  $D > 1$ , illustrating some degree of vertical propagation  
 480 occurred in all of them. The lowest values of  $\mathcal{R}$  coincide with the highest values of  $D$  in  
 481 systems where signatures of vertically propagating seiches were identified by Henderson  
 482 (2016) (Frains Lake and Sau reservoir) and where the vertical propagation was reported  
 483 (Lacamas Lake and La Fe reservoir). Lake Alpnach and Wood Lake are natural lakes with  
 484 nearly flat bottom and alike rectangular morphometries, so they have the highest  $\mathcal{R}$  and  $D \sim 1$ ,  
 485 with signatures of appreciable standing waves in the referred articles. The analysis supports  
 486 that vertically propagating basin-scale internal waves is the rule rather than the exception.

487 **Table 3.** Parameters of internal wave reflection in selected lakes. [1] Münnich et al. (1992),  
 488 [2] Lazerte (1980), [3] Serra et al. (2007), [4] Wiegand and Chamberlain (1987), [5]  
 489 Henderson and Deemer (2012), [6] present study.

Lake [source]	$L$ (m)	$H$ (m)	$N$ (Hz)	$T$ (h)	$v_{RMS}$ (m/s)	$D$	$\mathcal{R}$
Lake Alpnach [1]	5000	21.6	0.01	24	0.02	1.2	0.74
Frains Lake [2]	300	4	0.05	7	0.008	5.3	0.48
Sau reservoir [3]	3600	30	0.02	24	0.02	4.6	0.45
Wood Lake [4]	6800	26	0.02	24	0.02	2.1	0.80
Lacamas Lake [5]	1500	15	0.03	24	0.016	8.0	0.25 <sup>†</sup>
La Fe reservoir [6]	1000	20	0.02	20	0.01	9.2	0.41 <sup>†</sup>

490 <sup>†</sup>Directly estimated from the fit of a theoretical pattern to model or field results.

491

## 492 6. Conclusions

493 We used numerical modeling and theoretical inviscid wave ray tracing to explain  
 494 observations of vertical gradual phase shifting of temperature oscillations in a steep reservoir.  
 495 Due to the dominant supercritical reflection in the reservoir, 24-h period oscillations were  
 496 identified as vertically propagating internal seiches, characterized by high coherence  
 497 throughout the water column and gradual upward phase shifting of temperature and velocity

498 profiles, and standing waves of 24-h period did not form. For lower forcing frequencies,  
499 characteristic of higher order vertical modes, the supercritical reflection increases, so higher  
500 order vertical motions are more likely to occur as vertically propagating seiches and are less  
501 suitable to be described by standing mode theory.

502 We conclude that vertical propagating basin scale internal waves are ubiquitous to stratified  
503 lakes and reservoirs, due to the imperfect reflection of internal wave rays and viscous  
504 dissipation, whilst the non-dissipative modal description is a valid approximation in systems  
505 where subcritical reflection is significant, so the amount of upward propagating reflected  
506 energy is similar to the downward incident energy, despite some degree of vertical  
507 propagation always remains. The mechanisms described in this paper, which explain vertical  
508 propagation and standing mode preclusion, are expected to occur in any given lake, but their  
509 signatures are more evident in steep sided lakes, with a wide metalimnion and/or with a  
510 significant stratification extending through the water column. In some systems where  
511 significant supercritical reflection may be important, the modal description has been used  
512 with apparent success because the signature of vertically propagating waves is difficult to  
513 observe when there is a thin metalimnion separating well mixed epilimnion and hypolimnion.

514

## 515 **7. Acknowledgments**

516 The authors thank to Empresas Públicas de Medellín (EPM) for funding the field work and  
517 providing reservoir data.

518

519 **8. Data availability statement**

520 Software for this research is available in Hodges and Dallimore (2016) at  
521 <https://www.hydronumerics.com.au/software/aquatic-ecosystem-model-3d>. Configuration  
522 files for the simulations presented here and field data for this research will be available at a  
523 repository by the time of publication.

524

525

526 **9. References**

- 527 Boegman, L., J. Imberger, G. N. Ivey, and J. P. Antenucci. 2003. High-frequency internal  
528 waves in large stratified lakes. *Limnol. Oceanogr.* **48**: 895–919.
- 529 Cushman-Roisin, B., V. Tverberg, and E. G. Pavia. 1989. Resonance of internal waves in  
530 fjords: A finite-difference model. *J. Mar. Res.* **47**: 547–567.  
531 doi:10.1357/002224089785076190
- 532 Dauxois, T., A. Didier, and E. Falcon. 2004. Observation of near-critical reflection of internal  
533 waves in a stably stratified fluid. *Phys. Fluids* **16**: 1936–1941. doi:10.1063/1.1711814
- 534 Dissanayake, P., H. Hofmann, and F. Peeters. 2019. Comparison of results from two 3D  
535 hydrodynamic models with field data: internal seiches and horizontal currents. *Int.*  
536 *Waters* **9**: 239–260. doi:10.1080/20442041.2019.1580079
- 537 Evans, M. A., S. MacIntyre, and G. W. Kling. 2008. Internal wave effects on photosynthesis:  
538 Experiments, theory, and modeling. *Limnol. Oceanogr.* **53**: 339–353.  
539 doi:10.4319/lo.2008.53.1.0339
- 540 Gill, A. E. 1982. *Atmosphere-Ocean Dynamics*, Academic Press.
- 541 Gómez-Giraldo, A., J. Imberger, and J. P. Antenucci. 2006. Spatial structure of the dominant  
542 basin-scale internal waves in Lake Kinneret. *Limnol. Oceanogr.* **51**: 229–246.  
543 doi:10.4319/lo.2006.51.1.0229
- 544 Gómez-Giraldo, A., J. Imberger, J. P. Antenucci, and P. S. Yeates. 2008. Wind-shear-  
545 generated high-frequency internal waves as precursors to mixing in a stratified lake.  
546 *Limnol. Oceanogr.* **53**: 354–367. doi:10.4319/lo.2008.53.1.0354

547 Grinsted, A., J. C. Moore, and S. Jevrejeva. 2004. Application of the cross wavelet transform  
548 and wavelet coherence to geophysical time series. *Nonlinear Process. Geophys.* **11**:  
549 561–566. doi:10.5194/npg-11-561-2004

550 Henderson, S. M. 2016. Turbulent production in an internal wave bottom boundary layer  
551 maintained by a vertically propagating seiche. *J. Geophys. Res. Ocean.* **121**: 2481–2498.  
552 doi:10.1002/2015JC011071

553 Henderson, S. M., and B. R. Deemer. 2012. Vertical propagation of lakewide internal waves.  
554 *Geophys. Res. Lett.* **39**: n/a-n/a. doi:10.1029/2011GL050534

555 Hodges, B. R. 2000. Numerical Techniques in CWR-ELCOM (code release v. 1). CWR  
556 Manuscr. WP **1422**.

557 Hodges, B. R., and C. Dallimore. 2013. Estuary, Lake and Coastal Ocean Model: ELCOM  
558 v2. 2 science manual, Technical report, Centre for Water Research, Univ. of Western  
559 Australia.

560 Hodges, B. R., and C. Dallimore. 2016. Aquatic Ecosystem Model: AEM3D, v1. 0. User  
561 Manual, Hydronumerics, Aust. Melb.

562 Imam, Y. E., B. E. Laval, and G. a. Lawrence. 2013. The baroclinic response to wind in a  
563 small two-basin lake. *Aquat. Sci.* **75**: 213–233. doi:10.1007/s00027-012-0268-1

564 Imberger, J. 1998. Flux paths in a stratified lake : A review, p. 1–17. *In* J. Imberger [ed.],  
565 Physical Processes in lakes and oceans. Coastal and estuarine studies. V. 54. AGU.

566 Kocsis, O., B. Mathis, M. Gloor, M. Schurter, and A. Wüest. 1998. Enhanced mixing in  
567 narrows: A case study at the Mainau sill (Lake Constance). *Aquat. Sci.* **60**: 236–252.

568 doi:10.1007/s000270050039

569 de la Fuente, A., K. Shimizu, J. Imberger, and Y. Niño. 2008. The evolution of internal waves  
570 in a rotating, stratified, circular basin and the influence of weakly nonlinear and  
571 nonhydrostatic accelerations. *Limnol. Oceanogr.* **53**: 2738–2748.  
572 doi:10.4319/lo.2008.53.6.2738

573 de la Fuente, A., K. Shimizu, Y. Niño, and J. Imberger. 2010. Nonlinear and weakly  
574 nonhydrostatic inviscid evolution of internal gravitational basin-scale waves in a large,  
575 deep lake: Lake Constance. *J. Geophys. Res.* **115**: C12045. doi:10.1029/2009JC005839

576 Lazerte, B. D. 1980. The dominating higher order vertical modes of the internal seiche in a  
577 small lake. *Limnol. Oceanogr.* **25**: 846–854. doi:10.4319/lo.1980.25.5.0846

578 Lemckert, C., J. Antenucci, A. Saggio, and J. Imberger. 2004. Physical Properties of  
579 Turbulent Benthic Boundary Layers Generated by Internal Waves. *J. Hydraul. Eng.* **130**:  
580 58–69. doi:10.1061/(ASCE)0733-9429(2004)130:1(58)

581 Maas, L. R. M., and F.-P. A. Lam. 1995. Geometric focusing of internal waves. *J. Fluid*  
582 *Mech.* **300**: 1–41. doi:10.1017/S0022112095003582

583 Münnich, M., a. Wüest, and D. M. Imboden. 1992. Observations of the second vertical mode  
584 of the internal seiche in an alpine lake. *Limnol. Oceanogr.* **37**: 1705–1719.  
585 doi:10.4319/lo.1992.37.8.1705

586 Pernica, P., M. G. Wells, and W. G. Sprules. 2013. Internal waves and mixing in the  
587 epilimnion of a lake affects spatial patterns of zooplankton in a body-size dependent  
588 manner. *Limnol. Oceanogr. Fluids Environ.* **3**: 279–294. doi:10.1215/21573689-  
589 2409149

- 590 Phillips, O. 1977. *The Dynamics of the Upper Ocean*, 2nd ed. Cambridge Univ Press.
- 591 Posada-Bedoya, A., A. Gómez-Giraldo, and R. Román-Botero. 2022. Decoupled basin-scale  
592 internal waves in a continuously stratified two-basin tropical Andean reservoir.  
593 *Limnologica* **93**: 125931. doi:10.1016/j.limno.2021.125931
- 594 Posada-Bedoya, A., A. Gómez-Giraldo, and R. Román Botero. 2019. Preliminary  
595 characterization of the dominant baroclinic modes of a tropical Andean reservoir during  
596 a dry period. *Rev. la Acad. Colomb. Ciencias Exactas, Físicas y Nat.* **43**: 297.  
597 doi:10.18257/raccefy.799
- 598 Posada-Bedoya, A., A. Gómez-Giraldo, and R. Román-Botero. 2021. Effects of riverine  
599 inflows on the climatology of a tropical Andean reservoir. *Limnol. Oceanogr.*  
600 *lno.11897*. doi:10.1002/lno.11897
- 601 Román-Botero, R., A. Gómez-Giraldo, and M. T. Botero. 2013. Efecto estacional de los  
602 afluentes en la estructura térmica de un pequeño embalse neotropical, La Fe - Colombia.  
603 *Dyna* **80**: 152–161.
- 604 Serra, T., J. Vidal, X. Casamitjana, M. Soler, and J. Colomer. 2007. The role of surface  
605 vertical mixing in phytoplankton distribution in a stratified reservoir. *Limnol. Oceanogr.*  
606 **52**: 620–634. doi:10.4319/lo.2007.52.2.0620
- 607 Shimizu, K., and J. Imberger. 2008. Energetics and damping of basin-scale internal waves in  
608 a strongly stratified lake. *Limnol. Oceanogr.* **53**: 1574–1588.
- 609 Simpson, J. H., P. J. Wiles, and B. J. Lincoln. 2011. Internal seiche modes and bottom  
610 boundary-layer dissipation in a temperate lake from acoustic measurements. *Limnol.*  
611 *Oceanogr.* **56**: 1893–1906. doi:10.4319/lo.2011.56.5.1893

612 Sutherland, B. R. 2010. Internal Gravity Waves,.

613 Thorpe, S. a. 1998. Some dynamical effects of internal waves and the sloping sides of lakes.  
614 Phys. Process. Lakes Ocean. Coast. Estuar. Stud. **54**: 441–460.

615 Turner, J. S. 1973. Buoyancy Effects in Fluids, Cambridge University Press.

616 Ulloa, H. N., K. B. Winters, A. de la Fuente, and Y. Niño. 2015. Degeneration of internal  
617 Kelvin waves in a continuous two-layer stratification. J. Fluid Mech. **777**: 68–96.  
618 doi:10.1017/jfm.2015.311

619 UNESCO. 1981. Tenth report of the joint panel on oceanographic tables and standards. Tech.  
620 Pap. Mar. Sci. No. 36 24.

621 Vidal, J., and X. Casamitjana. 2008. Forced Resonant Oscillations as a Response to Periodic  
622 Winds in a Stratified Reservoir. J. Hydraul. Eng. **134**: 416–425.  
623 doi:10.1061/(ASCE)0733-9429(2008)134:4(416)

624 Vidal, J., S. MacIntyre, E. E. McPhee-Shaw, W. J. Shaw, and S. G. Monismith. 2013.  
625 Temporal and spatial variability of the internal wave field in a lake with complex  
626 morphometry. Limnol. Oceanogr. **58**: 1557–1580. doi:10.4319/lo.2013.58.5.1557

627 Wiegand, R. C., and V. Chamberlain. 1987. Internal waves of the second vertical mode in a  
628 stratified lake. Limnol. Oceanogr. **32**: 29–42. doi:10.4319/lo.1987.32.1.0029

629 Woodward, B. L., C. L. Marti, J. Imberger, M. R. Hipsey, and C. E. Oldham. 2017. Wind  
630 and buoyancy driven horizontal exchange in shallow embayments of a tropical  
631 reservoir: Lake Argyle, Western Australia. Limnol. Oceanogr. **62**: 1636–1657.  
632 doi:10.1002/lno.10522

633 Wüest, A., and A. Lorke. 2003. Small-Scale Hydrodynamics in Lakes. *Annu. Rev. Fluid*  
634 *Mech.* **35**: 373–412. doi:10.1146/annurev.fluid.35.101101.161220

635